

1 **Visibility-derived aerosol optical depth over global land from 1959 to** 2 **2021**

3 Hongfei Hao¹, Kaicun Wang², Chuanfeng Zhao³, Guocan Wu¹, Jing Li³

4 ¹Global Change and Earth System Science, Faculty of Geographical Science, Beijing Normal
5 University, Beijing 100875, China

6 ²Institute of Carbon Neutrality, Sino French Institute of Earth System Science, College Urban and
7 Environmental Sciences, Peking University, Beijing 100871, China

8 ³Institute of Carbon Neutrality, Department of Atmospheric and Oceanic Sciences, School of
9 Physics, College Urban and Environmental Sciences, Peking University, Beijing 100871, China

10 *Corresponding Author: Kaicun Wang (kcwang@pku.edu.cn)*

11 **Abstract**

12 Long-term and high spatial resolution aerosol optical depth (AOD) data are essential for climate
13 change detection and attribution. Global ground-based AOD observations are sparsely distributed,
14 and satellite AOD retrievals have a low temporal frequency, as well low accuracy before 2000 over
15 land. In this study, AOD at 550 nm is derived from visibility observations collected at more than
16 5000 meteorological stations over global land from 1959 to 2021. The AOD retrievals (550 nm) of
17 the Moderate Resolution Imaging Spectroradiometer (MODIS) onboard the Aqua Earth observation
18 satellite are used to train the machine learning model, and the ERA5 reanalysis boundary layer
19 height is used to convert the surface visibility to AOD. Comparison with independent dataset
20 (AERONET ground-based observations) shows that the predicted AOD has a correlation coefficient
21 of 0.55 at daily scale. The correlation coefficients are higher at monthly and annual scales, which
22 are 0.61 for the monthly and 0.65 for the annual, respectively. The evaluation shows consistent
23 predictive ability prior to 2000, with a correlation coefficient of 0.54, 0.66 and 0.66 at daily, monthly,
24 and annual scales, respectively. Due to a small number and sparse visibility stations prior to 1980,
25 the global/regional analysis in this study is from 1980 to 2021. From 1980 to 2021, the mean
26 visibility-derived AOD over the global land, the Northern Hemisphere, and the Southern
27 Hemisphere are 0.177, 0.178, and 0.175, with a trend of -0.0029/10a, -0.0030/10a, and -0.0021/10a
28 from 1980 to 2021. The regional means (trends) of AOD are 0.181 (-0.0096/10a), 0.163 (-
29 0.0026/10a), 0.146 (-0.0017/10a), 0.165 (-0.0027/10a), 0.198 (-0.0075/10a), 0.281 (-0.0062/10a),
30 0.182 (-0.0016/10a), 0.133 (-0.0028/10a), 0.222 (0.0007/10a), 0.244 (-0.0009/10a), 0.241 (0.0130
31 /10a), and 0.254 (0.0119/10a) in Eastern Europe, Western Europe, Western North America, Eastern
32 North America, Central South America, Western Africa, Southern Africa, Australia, Southeast Asia,
33 Northeast Asia, Eastern China, and India, respectively. However, the trends are decreasing
34 significantly in Eastern China (-0.0572/10a) and Northeast Asia (-0.0213/10a) after 2014 and the
35 larger increasing trend is found after 2005 in India (0.0446/10a). The visibility-derived daily AOD
36 dataset at 5032 stations over global land from 1959 to 2021 are available at National Tibetan Plateau
37 / Third Pole Environment Data Center (<https://doi.org/10.11888/Atmos.tpd.300822>) (Hao et al.,

38 2023).

39 How to cite. Hao, H., Wang, K., C. Zhao, Wu, G., J. Li (2023). Visibility-derived aerosol optical
40 depth over global land (1959-2021). National Tibetan Plateau / Third Pole Environment Data
41 Center. <https://doi.org/10.11888/Atmos.tpdc.300822>.

42 **1 Introduction**

43 Atmospheric aerosols are composed of solid and liquid particles suspended in the atmosphere.
44 Aerosol particles are directly emitted into the atmosphere or formed through gas-particle
45 transformation (Calvo et al., 2013), with diverse shapes and sizes (Fan et al., 2021), optical
46 properties, and components (Liao et al., 2015; Zhang et al., 2020; Li et al., 2022). Most atmospheric
47 aerosols are concentrated in the troposphere, especially in the boundary layer (Liu et al., 2022), with
48 a high concentration near emission sources (Kulmala et al., 2004), and a small portion are distributed
49 in the stratosphere. Atmospheric aerosols severely impact the atmospheric environment and human
50 health. They deteriorate air quality, reduce visibility, and cause other environmental issues (Wang
51 et al., 2012; Boers et al., 2015). They impair human health or other organisms' conditions by
52 increasing cardiovascular and respiratory disease incidence and mortality rates (Chafe et al., 2014;
53 Yang et al., 2022). The Global Burden of Disease shows that global exposure to ambient PM_{2.5}
54 (particulate matter suspended in air with an aerodynamic diameter of less than 2.5 micrometers)
55 resulted in 0.37 million deaths and 9.9 million disability-adjusted life years (Chafe et al., 2014).

56 Aerosols are inextricably linked to climate change. Atmospheric aerosols alter the Earth's energy
57 budget and affect the climate (Li et al., 2022). They cool the surface and heat the atmosphere by
58 scattering and absorbing solar radiation (Forster et al., 2007; Chen et al., 2022). Aerosols, such as
59 black carbon and brown carbon, also absorb solar radiation (Bergstrom et al., 2007), heat the local
60 atmosphere and suppress or invigorate convective activities (Ramanathan et al., 2001; Sun and Zhao,
61 2020). Aerosols also alter the optical properties and life span of clouds (Albrecht, 1989).
62 Atmospheric aerosols strongly affect regional and global short-term and long-term climates through
63 direct and indirect effects (Mcneill, 2017).

64 Tropospheric aerosols are considered as the second largest forcing factor for global climate change
65 (Li et al., 2022), and they reduce the warming due to greenhouse gases by -0.5°C (IPCC, 2021).
66 However, aerosols are also regarded as the largest contributor to the uncertainty of present-day
67 climate change attribution (IPCC, 2021). The uncertainties are caused by the deficiencies of the
68 global descriptions of aerosol optical properties (such as scattering and absorption) and
69 microphysical properties (such as size and component), and the impact on cloud and precipitation,
70 further affecting the estimation of aerosol radiative forcing (Lee et al., 2016; IPCC, 2021). Therefore,
71 sufficient aerosol observations are crucial. In aerosol measurements, aerosol optical depth (AOD)
72 is often used to describe its column properties, which represents the vertical integration of aerosol
73 extinction coefficients. AOD is an important physical quantity for estimating the content,
74 atmospheric pollution and climatology of aerosols (Zhang et al., 2020).

75 AOD data usually from ground-based and satellite-borne remote sensing observations. They have
76 both advantages and disadvantages. Ground-based lidar observation is an active remote sensing
77 technology. Lidar generally emits laser and receives backscattered signals to invert the extinction

78 coefficient of aerosols at different heights (Klett, 1985). By using the depolarization ratio, the type
79 of aerosol, such as fine particles or dust, can be distinguished (Bescond et al., 2013). The AOD
80 within a certain height can be calculated by integrating the extinction coefficients; however,
81 scattering signals are usually not received near the ground, leading to blind spots (Singh et al., 2019).
82 At present, there are many ground-based lidar worldwide and regional networks, which provides
83 important support of vertical changes in aerosols, such as the NASA Micro-Pulse Lidar Network
84 (MPLNET) in the early 1990s (Welton et al., 2002), the European Aerosol Research Lidar Network
85 (EARLINET) since 2000 (Bösenberg and Matthias, 2003), the Latin American Lidar Network
86 (LALINET) since 2013 (Guerrero-Rascado et al., 2016).

87 Ground-based remote sensing observations supply aerosol loading data (such as AOD), by
88 measuring the attenuation of radiation from the top of the atmosphere to the surface (Holben et al.,
89 1998). This type of observation mainly uses weather-resistant automatic sun and sky scanning
90 spectral radiometers to retrieve optical and microphysical aerosol properties (Che et al., 2014). The
91 Aerosol Robotic Network (AERONET) is a popular global network composed of NASA and
92 multiple international partners that provides high-quality and high-frequency aerosol optical and
93 microphysical properties under various geographical and environmental conditions (Holben et al.,
94 1998; Dubovik et al., 2000). The AERONET observations are extensively used to validate satellite
95 remote sensing observations and model simulations, as well as climatology study (Dubovik et al.,
96 2002b). There are many regional networks of sun photometers, such as the Maritime Aerosol
97 Network (MAN), which use a handheld sun photometer to collect data over the ocean and is merged
98 into AERONET (Smirnov et al., 2009), the China Aerosol Robot Sun Photometer Network
99 (CARSNET) (Che et al., 2009), the Canadian sub-network of AERONET (AEROCAN) (Bokoye et
100 al., 2001), Aerosol characterization via Sun photometry: Australian Network (AeroSpan)
101 (Mukkavilli et al., 2019), and the sky radiometer network (SKYNET) in Asia and Europe (Kim et
102 al., 2004; Nakajima et al., 2020). Another very valuable global network is the NOAA/ESRL
103 Federated Aerosol Network (FAN), which uses integrated nephelometers distinct from sun
104 photometers, mainly located in remote areas, providing background aerosol properties over 30 sites
105 (Andrews et al., 2019).

106 Satellite remote-sensing is a space-based method that can provide aerosol properties worldwide.
107 With the development of satellite remote sensing technology since 1970s, aerosol distributions can
108 be extracted with the advantage of sufficient real-time and global coverage from multiple satellite
109 sensors (Kaufman and Boucher, 2002; Anderson et al., 2005). The Advanced Very High Resolution
110 Radiometer (AVHRR) is the earliest sensor used for retrieving AOD over ocean (Nagaraja Rao et
111 al., 1989). The Moderate Resolution Imaging Spectroradiometer (MODIS), on board the Terra
112 (launched in 1999) and Aqua (launched in 2002) satellites is a popular sensor with 36 channels,
113 which have been used for AOD retrieval over both ocean and land based on the Dark Target and the
114 Deep Blue algorithms (Remer et al., 2005; Levy et al., 2013). The latest MODIS AOD data version
115 is the Collection 6.1, which provides global AOD over 20 years (Wei et al., 2019). There are also
116 many other satellite sensors that can be used to retrieve AOD, such as the Polarization and
117 Directionality of the Earth's Reflectances (POLDER) during 1996-1997, 2003 and 2004-2013
118 (Deuzé et al., 2000), Sea-viewing Wide Field-of-view Sensor (SeaWiFS) during 1997-2007
119 (O'reilly et al., 1998), the Multi-angle Imaging Spectroradiometer (MISR) on Terra since 1999
120 (Diner et al., 1998). The Cloud-Aerosol Lidar with Orthogonal Polarization (CALIOP) has also

121 derived aerosols in the vertical direction since 2006 (Winker et al., 2009).

122 These measurements provide important data for studying the global and regional spatiotemporal
123 variabilities and climate effect of aerosols. However, ground-based remote sensing observations
124 only provide aerosol properties with low spatial coverage. There were only about 150 ground
125 stations worldwide in 2002 and even fewer sites were available for climate analysis (Holben et al.,
126 1998; Chu et al., 2002), which limited aerosol climate research by spatial coverage (Bright and
127 Gueymard, 2019). Satellite remote sensing overcomes the limitations of spatial coverage. The
128 AVHRR has been used to retrieve AOD since 1980, but it is limited by a few channel number, low
129 spatial resolution, and insufficient validation through ground-based observations before 2000 (Hsu
130 et al., 2017). Many studies have only investigated the trends and distributions of aerosols after 2000
131 (Bösenberg and Matthias, 2003; Winker et al., 2013; Xia et al., 2016; Tian et al., 2023), because of
132 the lack of long-term and global cover AOD products, which is the bottleneck for aerosol climate
133 change detection and attributions.

134 To overcome these limitations and enrich aerosol data, alternative observation data could be utilized
135 to derive AOD. Atmospheric horizontal visibility is a suitable alternative (Wang et al., 2009; Zhang
136 et al., 2020), because it has the advantages of the long-term records with a large number of stations
137 worldwide.

138 Atmospheric visibility is a physical quantity that describes the transparency of the atmosphere
139 through manual and automatic observations, and the automatic observations of visibility usually
140 measure atmospheric extinction (scattering coefficient and transmissivity). Koschmieder (1924)
141 first proposed the relationship between the meteorological optical range and the total optical depth.
142 Elterman (1970) further established a formula between AOD and visibility by assuming an
143 exponential decrease in aerosol concentration with altitude, considering the extinction of molecules
144 and ozone to analyze air pollution, which called the Elterman model. Qiu and Lin (2001) corrected
145 the Elterman model by considering the influence of water vapor and used two water vapor pressure
146 correction coefficients to retrieve AOD of 16 stations in China in 1990. Wang et al. (2009) analyzed
147 the trend of AOD using visibility-based retrievals from 1973 to 2007 over land. Lin et al. (2014)
148 retrieved the AOD in eastern China in 2006 using visibility and aerosol vertical profiles provided
149 by GEOS-Chem. Wu et al. (2014) and Zhang et al. (2017) parameterized the constants in the
150 Elterman model and use satellite retrieved AOD to solve the parameters in the models at different
151 stations, to retrieve the long-term AOD in China.

152 Zhang et al. (2020) reviewed the methods of visibility retrieval of AOD, indicating that visibility-
153 based retrieval of AOD can compensate for the shortcomings of long-term aerosol observation data.
154 Simultaneously, various parameters, such as station altitude, consistency of visibility data, water
155 vapor and aerosol vertical profiles (scale height), were discussed with modified suggestions
156 proposed. These studies have enriched AOD data regionally. These studies have enriched aerosol
157 data in some extent. At present, there are very few studies on global visibility-retrieved AOD and to
158 analyze climatology of aerosols.

159 The two physical quantities of visibility and AOD have both connections and differences, making it
160 challenging to retrieve AOD from visibility. Visibility represents the maximum horizontal visible
161 distance near the surface which is impaired by surface aerosols, while AOD represents the total
162 column attenuation of solar radiation by aerosols from the surface to top of atmosphere. The

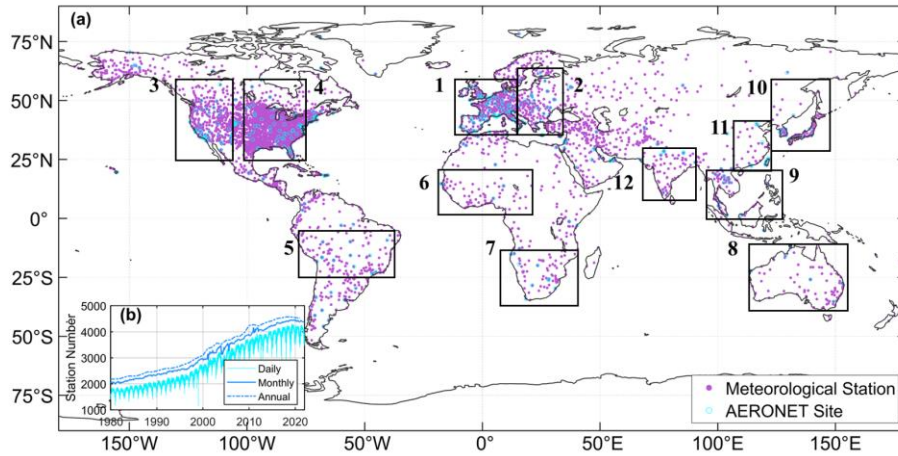
163 visibility of automatic observation is dependent on the local horizontal atmospheric extinction
164 (NOAA et al., 1998). Visibility has not a simple linear relationship with meteorological factors. The
165 vertical structure of aerosols is the greatest challenge to obtain, as it is not a simple hypothetical
166 curve in complex terrain and circulation conditions (Zhang et al., 2020). These limitations make it
167 more complex to derive AOD. Machine learning methods can effectively address complex nonlinear
168 relationships between variables and have been widely applied in remote sensing and climate
169 research fields. Li et al. (2021) used the random forest method to predict PM_{2.5} in Iraq and Kuwait
170 based on satellite AOD during 2001-2018. Kang et al. (2022) applied LightGBM and random forest
171 to estimate AOD over East Asia, and the results showed a consistency with AERONET. Dong et al.
172 (2023) derived aerosol single scattering albedo from visibility and satellite AOD over 1000 global
173 stations. Hu et al. (2019) used a deep learning method to retrieve horizontal visibility from MODIS
174 AOD. These studies have confirmed the ability of machine learning to effectively solve complex
175 relationships among variables. Previous studies are mostly conducted at the regional or national
176 scale, and few studies at the global scale. Thus, it is feasible to derive AOD from atmospheric
177 visibility over global land by using the machine learning method.

178 In this study, we propose a machine learning method to derive AOD, where satellite AOD is the
179 target value, and visibility and other related meteorological variables are the predictors. We explain
180 the model's robustness, and evaluate the model's predictive ability, and validate the model's
181 predictions using independent ground-based AOD, satellite retrievals and reanalysis AOD, and
182 analyze the mean and trend of AOD across land and regions. A station-scale dataset of long-term
183 AOD is generated. The Section 2 introduces the data and method. The Section 3 is the evaluation
184 and validation of the visibility-derived AOD, and the distribution and trends are discussed at global
185 and regional scales. The Section 5 presents the conclusions. This study is dedicated to supporting
186 the research of aerosols in climate change detection and attribution.

187 **2 Data and method**

188 **2.1 Study area**

189 The study area is global land. A total of 5032 meteorological stations and 395 AERONET sites are
190 selected in this study, shown in Figure 1. Twelve regions are selected for regional analysis, including
191 Eastern Europe, Western Europe, Western North America, Eastern North America, Central South
192 America, Western Africa, Southern Africa, Australia, Southeast Asia, Northeast Asia, Eastern China,
193 and India and the number of stations in the regions is 187, 494, 390, 1759, 132, 72, 78, 86, 76, 140,
194 26, and 51, respectively. The meteorological observations data including visibility are available
195 since 1959. The time period for global and regional analysis is from 1980 to 2021, during which the
196 visibility observations are sufficient with a uniform spatial distribution. As shown in Figure 1, the
197 number of active stations has exceeded 2000 during the period of 1980-1990 and the number of
198 active stations has exceeded 3000 since 2000.



199

200 **Figure 1:** Study area (a) and the meteorological station number (b) at daily, monthly, and annual
 201 scale. The number of meteorological stations (filled circles) is 5032. The number of AERONET
 202 sites (empty circles) is 395. The box regions of labelled with number 1-12 are Eastern Europe,
 203 Western Europe, Western North America, Eastern North America, Central South America, Western
 204 Africa, Southern Africa, Australia, Southeast Asia, Northeast Asia, Eastern China, and India.

205 2.2 Meteorological data

206 The ground-based hourly meteorological data from 1959 to 2021 is collected from 5032
 207 meteorological stations of airports over land, which can be downloaded at
 208 <https://mesonet.agron.iastate.edu/ASOS>. Over 1000 stations belong to the Automated Surface
 209 Observing System (ASOS), and others are sourced from airport reports around the world. The
 210 visibility measurements can be divided into automatic observation and manual observation.
 211 Automatic visibility observations reduce errors associated with human involvement in data
 212 collection, processing, and transmission. The visibility and other meteorological data are extracted
 213 from the Meteorological Terminal Aviation Routine Weather Report (METAR). The World
 214 Meteorological Organization (WMO) sets guidelines for METAR reports, including report format,
 215 encoding, observation instruments and methods, data accuracy, and consistency, which ensures the
 216 consistency and comparability of METAR reports globally. Some international regulations can be
 217 referenced at [https://community.wmo.int/en/implementation-areas-aeronautical-meteorology-](https://community.wmo.int/en/implementation-areas-aeronautical-meteorology-programme)
 218 [programme](https://community.wmo.int/en/implementation-areas-aeronautical-meteorology-programme).

219 The daily average visibility is calculated using harmonic mean in equation (1). The reciprocal of
 220 visibility is proportional to the extinction coefficient (Wang et al., 2009). Experiments have found
 221 that harmonic average visibility can better detect the weather phenomena than arithmetic average
 222 visibility, when visibility decline quickly (NOAA et al., 1998). Therefore, daily visibility will have
 223 greater representativeness.

$$224 \quad V = n / \left(\frac{1}{V_1} + \frac{1}{V_2} + \dots + \frac{1}{V_n} \right), \quad (1)$$

225 where V is the harmonic mean visibility, n is the daily record number, and V_1, V_2, \dots, V_n are the
 226 individual hourly visibility.

227 In addition to hourly visibility (VIS), other variables closely related to aerosol properties are selected,
228 including relative humidity (RH), dew point temperature (DT), temperature (TMP), wind speed
229 (WS) and sea-level pressure (SLP). Because air temperature affects atmospheric stability and the
230 rate of secondary particle formation, and humidity influences the size and hygroscopic growth, and
231 wind speed and pressure significantly impact the transport and deposition. Sky conditions (cloud
232 amount) and hourly precipitation are also selected to remove the records of extensive cloud cover
233 and precipitation.

234 We have processed the meteorological data as follows. The records with high missing value ratio
235 are eliminated (Husar et al., 2000). When over 80% overcast or fog, the records of sky conditions
236 are eliminated, though such situations occur less than 1% of the time over land (Remer et al., 2008).
237 The records with 1-hour precipitation greater than 0.1 mm are eliminated. We calculate the
238 temperature dew point difference (dT). The low visibility records under “blowing snow” weather
239 are eliminated at high latitude region ($> 65^{\circ}\text{N}$), when wind speed is great than 4.5m/s (Husar et al.,
240 2000). When the RH is greater than 90%, it is impossible to distinguish whether it is fog or haze, or
241 both, and even precipitation. Therefore, the records with the RH greater than or equal to 90% are
242 eliminated. When the RH is less than 30%, the hygroscopic effect of aerosols is very low or even
243 negligible. When the RH is between 30% and 90%, the hygroscopic effect of aerosols is high, and
244 visibility is converted to dry visibility (Yang et al., 2021c), as shown in equation (2). At least 3
245 hourly records of meteorological variables are required when calculating the daily average ($n \geq 3$).

$$246 \quad \mathbf{VISD} = \mathbf{VIS}/(\mathbf{0.26} + \mathbf{0.4285} * \mathbf{log}(100 - \mathbf{RH})), \quad (2)$$

247 where VISD is the dry visibility.

248 **2.3 Boundary layer height**

249 The hourly boundary layer height (BLH) data from 1980 to 2021 are available from the Fifth
250 Generation reanalysis of the European Medium-Range Weather Forecast Center (ERA5) with a
251 resolution of $0.25^{\circ} \times 0.25^{\circ}$ (<https://cds.climate.copernicus.eu>), which is the successor of ERA-
252 Interim and has undergone various improvements (Hersbach et al., 2020). The atmospheric
253 boundary layer is the layer closest to the Earth’s surface and exhibits complex turbulence activities,
254 and its height undergoes significant diurnal variation. The boundary layer plays a crucial role in
255 regulating and adjusting the distribution of atmospheric aerosols, such as vertical distribution,
256 concentration changes, transport, and deposition (Ackerman et al., 1995). The boundary layer height
257 serves as an approximate measure of the scale height for aerosols (Zhang et al., 2020).

258 Compared to observations of 300 stations over world from 2012 to 2019, the ERA5 BLH is
259 underestimated by 131.96m, and it is closest to the observations compared to JRA-55, and NECP-
260 2 BLH (Guo et al., 2021). The hourly BLH data is temporally and spatially matched with visibility
261 and other meteorological data before calculating the daily average.

262 Because the reciprocal of visibility is proportional to the extinction coefficient and positively related
263 to AOD (Wang et al., 2009), we calculate the reciprocal of visibility (VISI) and the reciprocal of dry
264 visibility (VISDI). Due to the influence of boundary layer height on the vertical distribution of
265 particles (Zhang et al., 2020), we calculate the product (VISDIB) of VISDI and BLH. Therefore,
266 the Predictor (Figure 2) is composed of 11 variables (TMP, Td, dT, RH, SLP, WS, VIS, BLH, VISI,
267 VISDI, and VISDIB).

268 **2.4 MODIS AOD products**

269 Satellite daily AOD data are available from the Moderate Resolution Imaging Spectroradiometer
270 (MODIS) Level 3 Collection 6.1 AOD products of the Aqua (MYD09CMA) satellite from 2002 to
271 2021 and Terra (MOD09CMA) satellite from 2000 to 2021 with a spatial resolution of $0.05^\circ \times 0.05^\circ$
272 at a wavelength of 550 nm (<https://ladsweb.modaps.eosdis.nasa.gov>). Terra (passing 10:30 am at
273 local time) and Aqua (passing 1:30 pm at local time) are successfully launched in December 1999
274 and May 2002, respectively. MODIS, carried on the Terra and Aqua satellites is a crucial instrument
275 in the NASA Earth Observing System program, which is designed to observe global biophysical
276 processes (Salomonson et al., 1987). The 2330 km-wide swath of the orbit scan can cover the entire
277 globe every one to two days. MODIS has 36 channels and more spectral channels than previous
278 satellite sensors (such as AVHRR). The spectrum ranges from 0.41 to 15 μm representing three
279 spatial resolutions: 250 m (2 channels), 500 m (5 channels), and 1 km (29 channels). The aerosol
280 retrievals use seven of these channels (0.47–2.13 μm) to retrieve aerosol characteristics and use
281 additional channels in other parts of the spectrum to identify clouds and river sediments. Therefore,
282 it has the ability to characterize the spatial and temporal characteristics of the global aerosol field.

283 The MODIS aerosol product actually uses different algorithms to retrieve aerosols over land. The
284 Dark Target (DT) algorithm is applied to densely vegetated areas because the surface reflectance
285 over dark-target areas is lower in the visible channels and has nearly fixed ratios with the surface
286 reflectance in the shortwave and infrared channels (Levy et al., 2007; Levy et al., 2013). The Deep
287 Blue (DB) algorithm is originally applied to bright land surfaces (such as deserts), and later extended
288 to cover all cloud-free and snow-free land surfaces (Hsu et al., 2006; Hsu et al., 2013). MODIS
289 Collection 6.1 aerosol product is released in 2017, incorporating significant improvements in
290 radiometric calibration and aerosol retrieval algorithms.

291 The aerosol retrievals usually are evaluated by the expected error. For the DT algorithm, the
292 expected error is $\pm (0.05 + 15\% \text{AOD}_{\text{AERONET}})$. The coverage of retrieval products varies by season
293 based on the DT algorithm over land. Higher spatial coverage is observed in August and September,
294 reaching 86-88%. During December and January, due to the presence of permanent ice and snow
295 cover in high-latitude regions of the Northern Hemisphere, the spatial coverage is 78-80%. Thus,
296 challenges remain in retrieving AOD values in high-latitude regions (Wei et al., 2019). However,
297 visibility observations are available in high-latitude regions, thereby partially addressing the lack in
298 these regions. In this study, the Terra and Aqua MODIS AOD are temporally and spatially matched
299 with the meteorological stations. Aqua MODIS AOD is used as the Target when training the model,
300 and Terra MODIS AOD is used in the evaluation and validation of the model results, as shown in
301 the flowchart (Figure 2).

302 **2.5 Ground-based AOD**

303 Ground-based 15-minute AOD observations are available from the Aerosol Robotic Network
304 (AERONET) Version 3.0 Level 2.0 product at 395 sites (Figure 1), which can be downloaded from
305 <https://aeronet.gsfc.nasa.gov>. The AERONET program is a federation of ground-based remote
306 sensing aerosol networks established by NASA and PHOTONS, including many subnetworks (such
307 as AeroSpan, AEROCAN, NEON, and CARSNET). The sun photometer (CE-318) measures
308 spectral sun and sky irradiance in the 340-1020 nm spectral range. AERONET has three levels of
309 AOD products: Level 1.0 (unscreened), Level 1.5 (cloud screened), and Level 2.0 (cloud screened
310 and quality assured). Compared to Version 2, the Version 3 Level 2.0 database has undergone further

311 cloud screening and quality assurance, which is generated based on Level 1.5 data with pre- and
312 post-calibration and temperature adjustment and is recommended for formal scientific research
313 (Giles et al., 2019). AERONET provides AOD products at wavelengths of 440, 675, 870, and 1020
314 nm. When the aerosol loading is low, the error is significant. When the AOD at 440 nm wavelength
315 is less than 0.2, the error is 0.01, which is equivalent to the error of the absorption band in the total
316 optical depth (Dubovik et al., 2002a). The total uncertainty in AOD under cloud-free conditions is
317 less than ± 0.01 , when the wavelength is more than 440 nm, and ± 0.02 when the wavelength is less
318 than 440 nm (Holben et al., 1998). AERONET AOD is usually considered as the ‘true’ value. The
319 AOD at 440 nm and the Ångström index at 440–675 nm are used to calculate AOD at 550 nm (not
320 provided by AERONET), as shown in equation (3).

$$321 \quad \tau_{550} = \tau_{440} \left(\frac{550}{440} \right)^{-\alpha}, \quad (3)$$

322 where τ_{440} and τ_{550} are the AOD at a wavelength of 440 nm and 550 nm, and α is the Ångström
323 index.

324 The daily average AOD requires at least two observations within 1 hour (± 30 minutes) of
325 Aqua/Terra transit time (Wei et al., 2019). The matching conditions between AERONET sites and
326 meteorological stations are (1) a distance of less than 0.5 °, and (2) at least three years of
327 observations. Finally, a total of 395 sites are selected.

328 **2.6 AOD reanalysis dataset**

329 The monthly AOD (550 nm) dataset of Modern-Era Retrospective Analysis for Research and
330 Applications version 2 (MERRA-2) from 1980 to 2021 is a NASA reanalysis of the modern satellite
331 era produced by NASA’s Global Modeling and Assimilation Office with a spatial resolution of
332 $0.5 \times 0.625^\circ$ (Gelaro et al., 2017), available at <https://disc.gsfc.nasa.gov>. MERRA-2 AOD uses an
333 analysis splitting technique to assimilate AOD data at 550 nm. The assimilated AOD observations
334 are including (1) AOD retrievals from AVHRR (1979–2002) over global ocean, (2) AOD retrievals
335 from MODIS on Terra (2000–present) and Aqua (2002–present) over global land and ocean, (3)
336 AOD retrievals from MISR (2000–2014) over bright and desert surfaces, and (4) direct AOD
337 measurements from the ground-based AERONET (1999–2014) (Gelaro et al., 2017). The monthly
338 MERRA-2 AOD is used to evaluate the model’s predictive ability before 2000 and after 2000.

339 **2.7 Decision tree regression**

340 **2.7.1 Feature selection**

341 Although a multidimensional dataset can provide as much potential information as possible for
342 AOD, irrelevant and redundant variables can also introduce significant noise in the model and
343 reduce the model’s accuracy and stability (Kang et al., 2021; Dong et al., 2023). Therefore, the F-
344 test is used to search for the optimal feature subset in the Predictor, aiming to eliminate irrelevant
345 or redundant features and select truly relevant features, which helps to simplify the model’s input
346 and improve the model’s prediction ability (Dhanya et al., 2020). The F-test is a statistical test that
347 gives an f-score ($= -\log(p)$, p represents the degree to which the null hypothesis is not rejected) by
348 calculating the ratio of variances. In this study, we calculate the ratio of variance between the
349 Predictors and Target, and the features are ranked based on the f-score values. A larger value of f-

350 score means that the distances between Predictors and Target are less and the relationship is closer,
351 thus, the feature is more important. We set $p=0.05$. When the score is less than $-\log(0.05)$, the
352 variable in the Predictors is not considered.

353 **2.7.2 Data balance**

354 When the weather is clear, the AOD value is small ($AOD < 0.5$), and the variability of AOD is small, and
355 the data is concentrated near the mean value. When heavy pollution, the AOD value is large ($AOD > 0.5$).
356 Compared to clear sky, the AOD sequence will show "abnormal" large values with low frequency, which
357 is a phenomenon of imbalance AOD data. When dealing with imbalanced datasets, because of the
358 tendency of machine learning algorithms to perform better on the majority class and overlook the
359 minority class, the model may be underfit (Chuang and Huang, 2023). Data augmentation techniques are
360 commonly employed to address the issue in imbalance data, which applies a series of transformations or
361 expansions to generate new training data, thereby increasing the diversity and quantity of the training
362 data of the minority class.

363 The Adaptive Synthetic Sampling (ADASYN) is a data augmentation technique specifically designed to
364 address data imbalance problem (He et al., 2008; Mitra et al., 2023). It is an extension of the Synthetic
365 Minority Over-sampling Technique (SMOTE) algorithm (Fernández et al., 2018). The goal of ADASYN
366 is to generate synthetic sample data for the minority class to increase its representation in the dataset.
367 ADASYN, which adaptively adjusts the generation ratio of synthetic samples based on the density
368 distribution of sample data, improves the dataset balance and enhances the performance of machine
369 learning models in dealing with imbalanced data.

370 The processing of imbalanced data includes (1) AOD sequences are classified into three types based on
371 percentile (0-1%, 2% -98%, 99%), (2) When the mean of the third type of AOD is greater than 5 times
372 the standard deviation of the second type, it is considered an imbalanced sequence. These data, with a
373 total amount less than 5% of the sample, are imbalanced data, and (3) Then synthetic samples are
374 generated with a 10% upper limit of the original samples.

375 **2.7.3 Decision tree regression model**

376 The decision tree is a machine learning algorithm based on a tree-like structure used to solve
377 classification and regression problems. We use regression tree algorithm to construct a regression model
378 by analyzing the mapping relationship between object attributes (Predictor) and object values (Target).
379 The internal nodes have binary tree structures with feature values of "yes" and "no". In addition, each
380 leaf node represents a specific output for a feature space. The advantages of the regression tree include
381 the ability to handle continuous features and the ease of understanding the generated tree structure
382 (Teixeira, 2004; Berk, 2008). Before training the tree model, the variables (Input) are normalized to
383 improve model performance, and after prediction, the results are obtained by denormalization. The 10-
384 fold cross-validation method is employed to improve the generalization ability of the model (Browne,
385 2000).

386 The core problems of the regression tree need to be solved are to find the optimal split variable and
387 optimal split point. The optimal split point of Predictors is determined by the minimum MSE, which in
388 turn determines the optimal tree structure. We set $Y = [y_1, y_2, \dots, y_N]$ as the Target. We set $X =$
389 $[x_1, x_2, \dots, x_N]$ as the Predictors, $x_i = (x_i^1, x_i^2, \dots, x_i^n)$, $i = 1, 2, 3, \dots, N$, where n is the feature number, and
390 N is the length of sample. We set a training dataset as $D = [(x_1, y_1), (x_2, y_2), \dots, (x_N, y_N)]$.

391 A regression tree corresponds to a split in the feature space and the output values on the split domains.
 392 Assuming that the input space has been divided into M domains $[R_1, R_2, \dots, R_M]$ and there is a fixed
 393 output value on each R_M domain, the regression tree model can be represented as follows:

$$394 \quad f(x) = \sum_{m=1}^M c_m I(x \in R_m), m = 1, 2, \dots, M, \quad (4)$$

395 where I is the indicator function, equation (5):

$$396 \quad I = \begin{cases} 1, & x \in R_m \\ 0, & x \notin R_m \end{cases}, \quad (5)$$

397 When the partition of the input space is determined, the square error can be used to represent the
 398 prediction error of the regression tree for the training data, and the minimizing square error is used to
 399 solve the optimal output value on each domain. The optimal value (\widehat{c}_m) on a domain is the mean of the
 400 outputs corresponding to all input, namely:

$$401 \quad \widehat{c}_m = \text{ave}(y_i | x_i \in R_m), \quad (6)$$

402 A heuristic method is used to split the feature space. After each split, all values of all features in the
 403 current set are examined individually, and the optimal one is selected as the split point based on the
 404 principle of minimum sum of the square errors. The specific step is described as follows: for the training
 405 dataset, we recursively divide each region into two sub domains and calculate the output values of each
 406 sub domain; then, construct a binary decision tree. For example, split variable is x^j and split point is s .
 407 Then, in the domain $R_1(j, s) = [x | x^j \leq s]$ and domain $R_2(j, s) = [x | x^j > s]$, we can solve the loss
 408 function $L(j, s)$ to find the optimal j and s .

$$409 \quad L(j, s) = \sum_{x_i \in R_1(j, s)} (y_i - c_1)^2 + \sum_{x_i \in R_2(j, s)} (y_i - c_2)^2, \quad (7)$$

410 When $L(j, s)$ is the smallest, x^j is the optimal split variable and s is the optimal split point for the
 411 x^j .

$$412 \quad \min_{j, s} \left[\min_{c_1} \sum_{x_i \in R_1(j, s)} (y_i - c_1)^2 + \min_{c_2} \sum_{x_i \in R_2(j, s)} (y_i - c_2)^2 \right], \quad (8)$$

413 We use the optimal split variable x^j and the optimal split point s to split the feature space and calculate
 414 the corresponding output value.

$$415 \quad \widehat{c}_1 = \text{ave}(y_i | x_i \in R_1(j, s)), \quad \widehat{c}_2 = \text{ave}(y_i | x_i \in R_2(j, s)), \quad (9)$$

416 We traverse all input variables to find the optimal split variable x^j , forming a pair (j, s) . Divide the
 417 input space into two regions accordingly. Next, repeat the above process for each region until the stop
 418 condition is met. The regression tree is generated.

419 Therefore, the regression tree model $f(x)$ can be represented as follows:

$$420 \quad f(x) = \sum_{m=1}^M \widehat{c}_m I(x \in R_m), m = 1, 2, \dots, M, \quad (10)$$

421 2.8 Evaluation metrics

422 Evaluation metrics, including Root Mean Squared Error (RMSE), Mean Absolute Error (MAE) and
 423 Pearson Correlation Coefficient (R), are used to evaluate the performance and accuracy of the model

424 results.

425
$$RMSE = \sqrt{\frac{1}{n} \sum_{i=1}^n (y_i - \hat{y}_i)^2}, \quad (11)$$

426
$$MAE = \frac{1}{n} \sum_{i=1}^n |y_i - \hat{y}_i|, \quad (12)$$

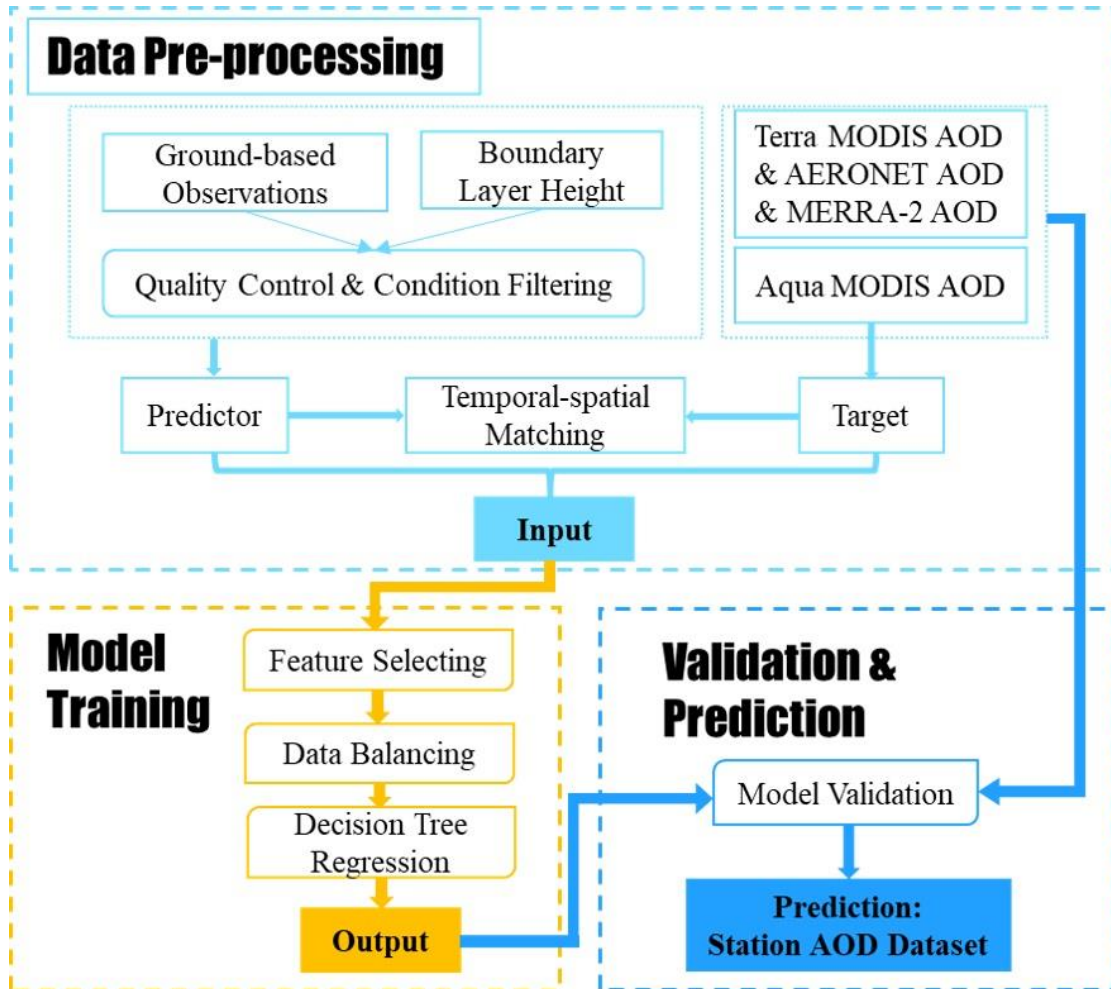
427
$$R = \frac{\sum_{i=1}^n (y_i - \bar{y})(\hat{y}_i - \bar{\hat{y}})}{\sqrt{(\sum_{i=1}^n (y_i - \bar{y})^2 \sum_{i=1}^n (\hat{y}_i - \bar{\hat{y}})^2)}}, \quad (13)$$

428 where y_i and \bar{y} are the predicted value and the average of the predicted values. \hat{y}_i and $\bar{\hat{y}}$ are
 429 the target and the average of the target. $i = 1, 2, \dots, n$. n is the length of sample.

430 The expected error (EE) is used to evaluate the AOD derived from visibility.

431
$$EE = \pm (0.05 + 0.15 * \tau_{true}), \quad (14)$$

432 where τ_{true} is the AOD at 550 nm from AERONET, satellite and reanalysis datasets.



433

434 **Figure 2:** Flowchart for deriving aerosol optical depth (AOD).

435 **2.9 Workflow**

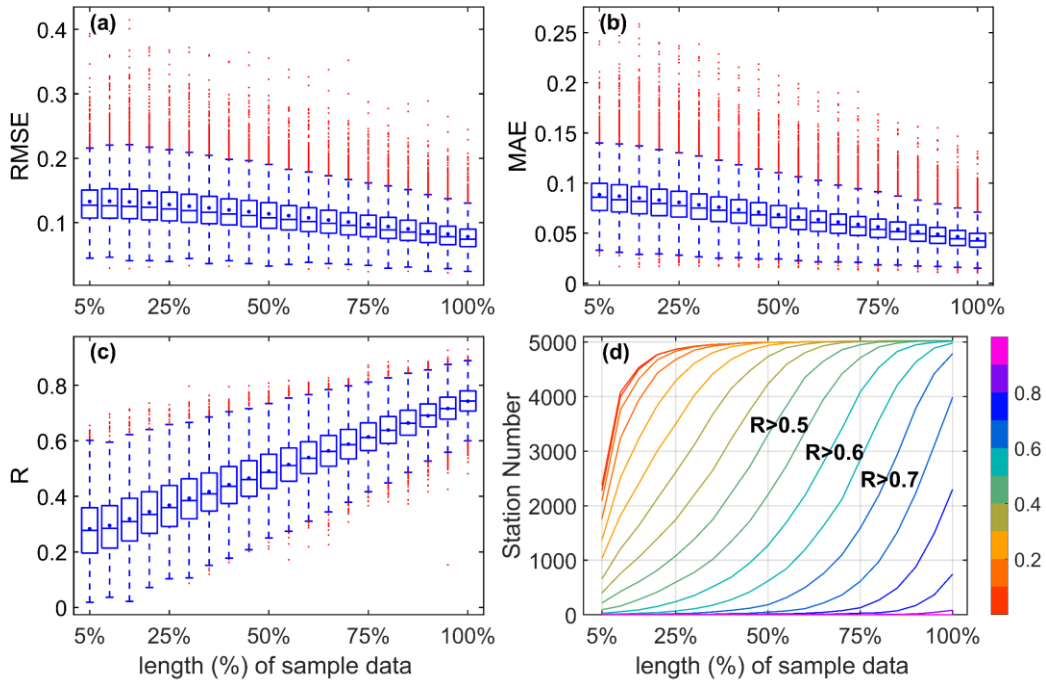
436 Figure 2 summarizes the flowchart and provides an overview of the structure of this study, which

437 involves four main parts: (1) data preprocessing, (2) model training, and (3) validation and
438 prediction.

439 3 Results and discussion

440 3.1 Dependence of model performance on training data length

441



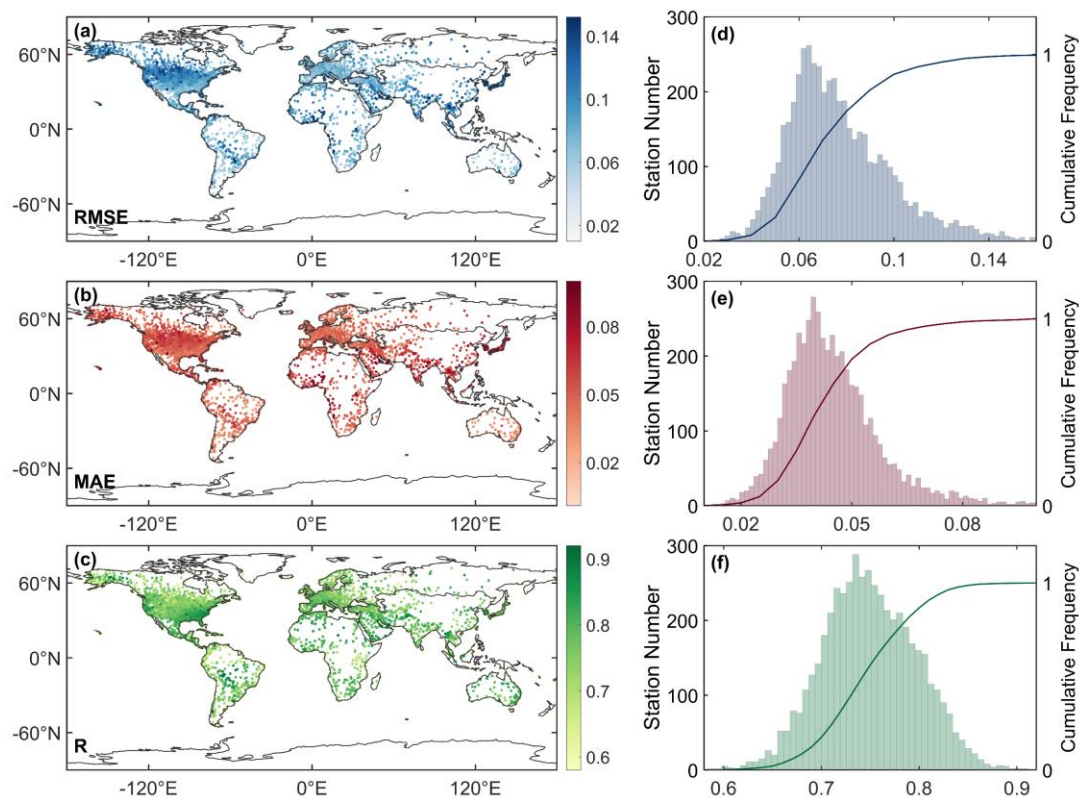
442

443 **Figure 3:** Boxplots of root mean squared error (RMSE) (a), mean absolute error (MAE) (b), and
444 correlation coefficient (R) (c) between predicted values and target using different lengths of sample
445 data (5% interval) as the training dataset, and the correlation coefficient curve (d) of the station
446 number and lengths of sample data.

447 We build the models using different lengths of sample data (5% to 100%, with a 5% interval) by random
448 allocation without overlap and evaluate the predictive performance of each model. Figure 3 (a-c) depicts
449 RMSE, MAE, and R between the predicted values and target based on the training data of 5% to 100%
450 sample data at a station. As the volume of the training data increases, the RMSE and MAE values
451 decrease, and the R values increase. Compared to 5% of the sample data, the result of 100% sample data
452 shows a decrease in RMSE by 41.1%, a decrease in MAE by 50.1%, and an increase in R by 162.3%.
453 The relationship between the length of sample data and the model's performance is positive for each
454 station. Figure 3 (d) shows that R of approximately 70% stations is greater than 0.5 at 50% of the sample
455 data, while at 75%, the R of approximately 80% of stations is greater than 0.6. When 100% of the sample
456 data is used as sample data, the R of approximately 80% of stations is greater than 0.75, and the R of
457 about 97% is greater than 0.7. This finding indicates that the predictive capability and robustness of the
458 model increase as the amount of training data increases. It may be attributed to the model's ability to
459 capture more complex patterns and relationships among the input by multi-year data.

460 3.2 Evaluation of model training performance

461 Figure 4 shows the spatial distribution (a-c) and frequency and cumulative frequency (d-e) of RMSE,
462 MAE, and R of all stations. The mean values of RMSE, MAE and R are 0.078, 0.044, and 0.750,
463 respectively. The RMSE of 93% stations is less than 0.11, the MAE of 91% is less than 0.06, and the R
464 of 88% is greater than 0.7. The R values in Africa, Asia, Europe, North America, Oceania, and South
465 America are 0.763, 0.758, 0.736, 0.750, 0.759, and 0.738, respectively. Although the RMSE and MAE
466 of a few stations are high in America and Asia, the R is still high (> 0.6). Therefore, the results of the
467 model's errors demonstrate that the model performs well on almost all stations.



468 **Figure 4:** Spatial distribution (a-c) of root mean squared error (RMSE), mean absolute error (MAE),
469 and correlation coefficient(R) between the model's result and target with 100% sample data. Station
470 number (bar) and cumulative frequency (curve) (d-e) of RMSE, MAE, and R.
471

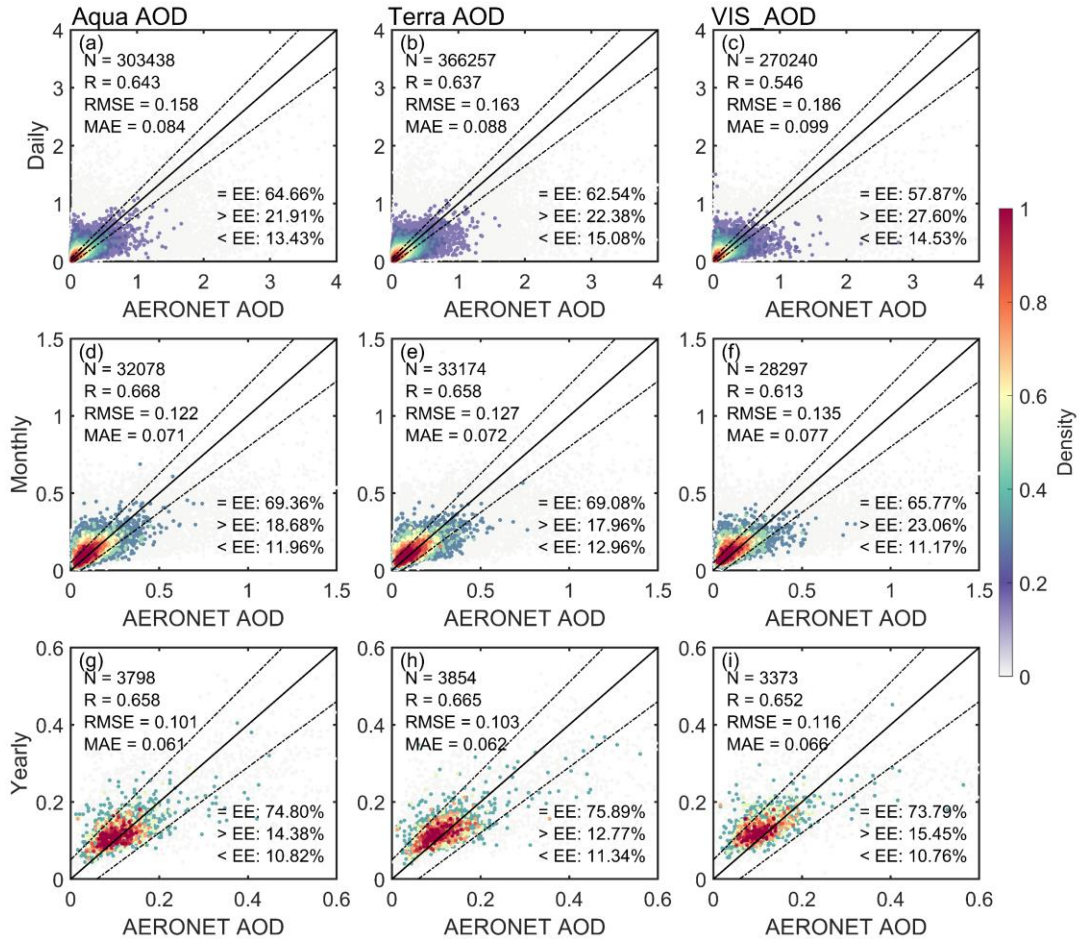
472 3.3 Validation and comparison with MODIS and AERONET AOD

473 3.3.1 Validation over global land

474 To validate the model's predictive ability, the visibility-derived AOD (for short, VIS_AOD) is compared
475 with Aqua, Terra, MERRA-2 and AERONET AOD at 550 nm for the global scale. Among them, Aqua
476 AOD has been used as training data, which is not an independent dataset. Terra AOD and AERONET
477 AOD have not been used as training data and can be regarded as independent datasets.

478 First, the relationship among daily MODIS and AERONET AOD is evaluated, as shown in Figure 5 (a-
479 b, d-e, g-h). The R values with Aqua AOD and Terra AOD are 0.643 and 0.637 on the daily scale, and
480 0.668 and 0.658 on the monthly scale, 0.658 and 0.665 on the yearly scale. The RMSE with Aqua AOD
481 and Terra AOD are 0.158 and 0.163 on the daily scale, and 0.122 and 0.127 on the monthly scale, 0.101

482 and 0.103 on the yearly scale. The MAE values with Aqua AOD and Terra AOD are 0.084 and 0.088 on
 483 the daily scale, and 0.071 and 0.072 on the monthly scale, 0.061 and 0.062 on the yearly scale. The
 484 percentages of sample point falling within the EE envelopes are 64.66% and 62.54% on the daily scale,
 485 and 69.36% and 69.08% on the monthly scale, 74.80% and 75.89% on the yearly scale.



486

487 **Figure 5:** Scatter density plots between AERONET AOD (550 nm) and Aqua MODIS AOD, Terra
 488 MODIS AOD and VIS_AOD on the daily (a-c), monthly (d-f) and yearly (g-i) scale. The solid black line
 489 represents the 1:1 line and the dashed lines represents expected error (EE) envelopes. The sample size
 490 (N), correlation coefficient (R), mean absolute error (MAE), and root mean square error (RMSE) are
 491 given. ‘= EE’, ‘> EE’, and ‘< EE’ represent the percentages (%) of retrievals falling within, above, and
 492 below the EE, respectively. The matching time for Aqua AOD and VIS_AOD with AERONET AOD is
 493 13.30 (\pm 30 minutes) at local time, and the matching time between Terra AOD and AERONET AOD is
 494 10.30 (\pm 30 minutes) at local time.

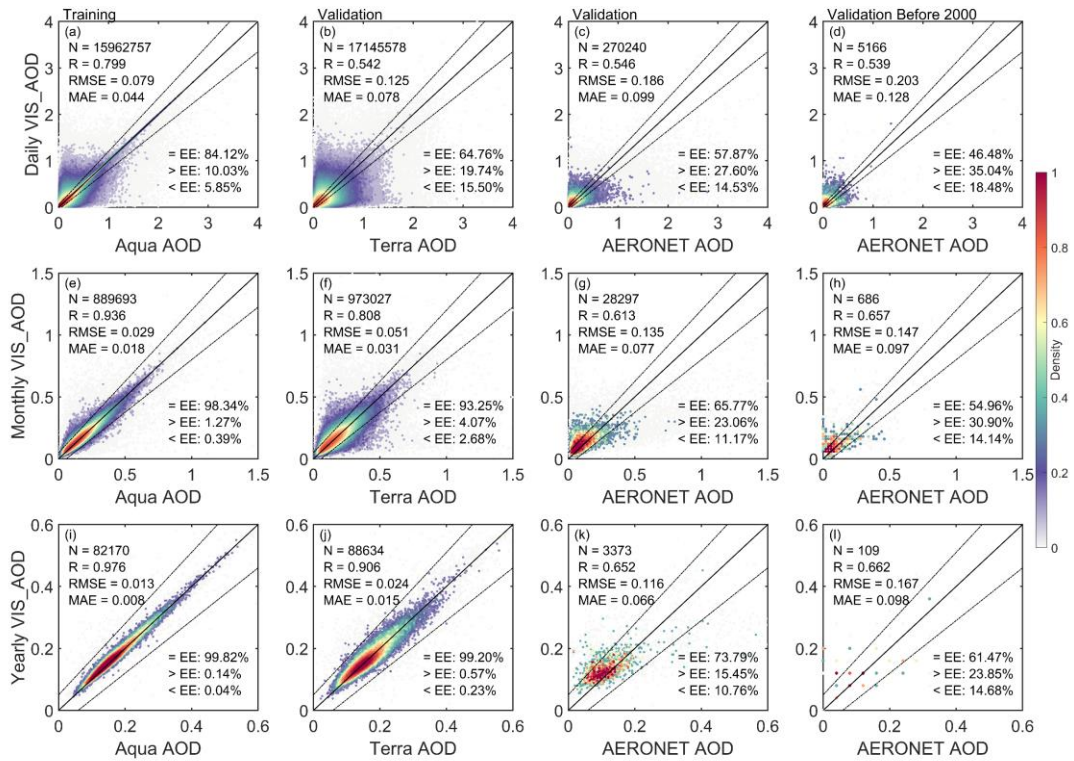
495 Figure 6 shows the scatter density plots and the EEs between VIS_AOD and Aqua AOD, Terra AOD,
 496 and AERONET AOD. Aqua AOD is not an independent validation, and Terra and AERONET AOD are
 497 independent validation. For the daily scale, the R, RMSE and MAE of between VIS_AOD and Aqua
 498 AOD (15,962,757 pairs data) is 0.799, 0.079 and 0.044, respectively. The percentage of sample point
 499 falling within the EE envelopes is 84.12% on the global scale (Figure 6 a). The R between VIS_AOD
 500 and Terra AOD (17,145,578 pairs data) is 0.542, with a RMSE of 0.125 and MAE of 0.078. The
 501 percentage falling within the EE envelopes is 64.76% (Figure 6 b). The R between VIS_AOD and

502 AERONET AOD (270,240 pairs data) at 395 sites is 0.546, with a RMSE of 0.186 and MAE of 0.099.
503 The percentage falling within the EE envelopes is 57.87% (Figure 6 c).

504 For the monthly and yearly scales, RMSE and MAE show a significant decrease between VIS_AOD and
505 Aqua, Terra, and AERONET AOD, and R and percentages falling within EE show a significant increase
506 in Figure 6 (e-g, i-k). The monthly RMSEs are 0.029, 0.051, and 0.135, the monthly MAEs are 0.018,
507 0.031, and 0.077, and the monthly R values are 0.936, 0.808, and 0.613, respectively. The percentages
508 falling within the EE envelopes are 98.34%, 93.25%, and 65.77%. The RMSEs on the yearly scale are
509 0.013, 0.024, and 0.116, the MAEs are 0.008, 0.015, and 0.066, and the R values are 0.976, 0.906, and
510 0.652, respectively. The percentages falling within the EE envelopes are 99.82%, 99.20%, and 73.79%.
511 The percentage falling within the EE envelopes against AERONET is smaller than that against Terra,
512 which may be related to the elevation of AERONET sites, the distance between AERONET and
513 meteorological stations, and observed time. The results highlighted above demonstrate a clear
514 improvement in performance on the monthly and yearly scales compared to the daily scale.

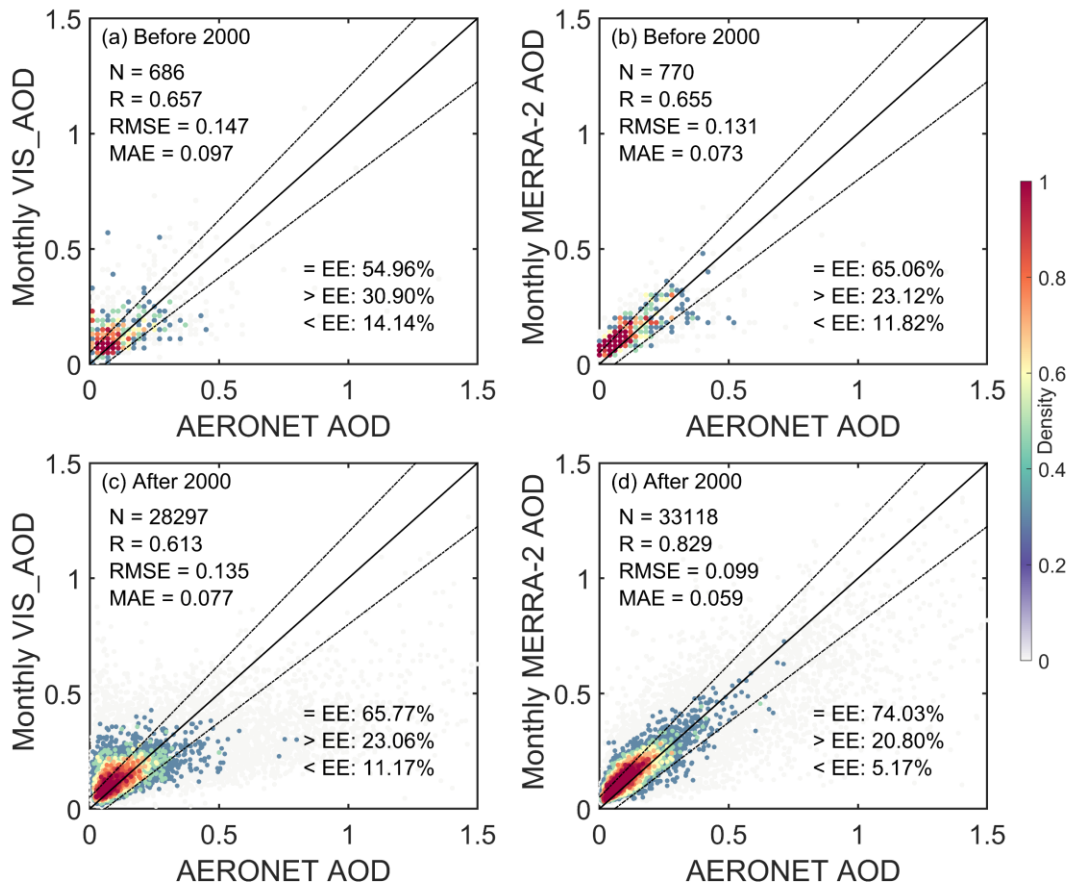
515 To further examine the predictive capability of historical data, we compare the VIS_AOD with
516 AERONET AOD before 2000, as shown in Figure 6 (d, h, l). We match 43 AERONET sites, with a total
517 of 5166 daily records. The result indicates that the daily-scale R is close to that after 2000 (Figure 6 c),
518 with the percentages approaching 50% falling within the EE envelopes. The monthly and annual
519 correlation coefficients are even higher, with a percentage of 55% falling within the EE envelopes.
520 Although the sample size is small, it still demonstrates the excellent predictive ability of the model.
521 Compared with AERONET (an independent validation dataset), the performance of VIS_AOD is almost
522 unchanged before and after 2000.

523 We also compare the VIS_AOD with the MERRA-2 reanalysis AOD on the monthly scale, as shown in
524 Figure 7. The correlation coefficient between MERRA-2 and AERONET is 0.655 before 2000, slightly
525 lower than the correlation coefficient (0.657) between VIS_AOD and AERONET. The correlation
526 coefficient between MERRA-2 and AERONET is 0.829 after 2000, significantly higher than that before
527 2000, while the correlation coefficient between VIS_AOD and AERONET is 0.613. It suggests that
528 VIS_AOD and MERRA-2 AOD have similar accuracy before 2000. The correlation of MERRA-2 after
529 2000 is higher and even performs better than MODIS retrievals (as shown in Figure 5) when evaluated
530 at AERONET sites. However, before 2000, the correlation coefficient of MERRA-2 and AERONET,
531 RMSE, and MAE all show significant changes and differences in consistency. The higher correlation
532 between MERRA-2 and AERONET AOD is partly because MERRA-2 has assimilated AERONET AOD
533 observations (Gelaro et al., 2017). Compared to AERONET, VIS_AOD and Aqua/Terra MODIS have a
534 similar correlation coefficient. The correlation coefficient of VIS_AOD before 2000 is even higher than
535 after 2000, and the changes in RMSE and MAE are not significant. It indicates good consistency of
536 VIS_AOD. In conclusion, the predicted results have good consistency with AERONET AOD and Terra
537 AOD on the daily scale. The monthly and annual results have a significant improvement. The model
538 shows good predictive capabilities before/after 2000, highlighting the stable accuracy of VIS_AOD.



539

540 **Figure 6:** Scatter density plots between predicted AOD (VIS_AOD) and Aqua MODIS AOD, Terra
 541 MODIS AOD, AERONET AOD and AERONET AOD before 2000 on the daily (a-d), monthly (e-h) and
 542 yearly (g-i) scale. The solid black line represents the 1:1 line and the dashed lines represents expected
 543 error (EE) envelopes. The sample size (N), correlation coefficient (R), mean absolute error (MAE), and
 544 root mean square error (RMSE) are given. ‘= EE’, ‘> EE’, and ‘< EE’ represent the percentages (%) of
 545 retrievals falling within, above, and below the EE, respectively. Note Aqua AOD is not an independent
 546 validation dataset for predicted results, while Terra and AERONET AOD are independent validation
 547 datasets.



548

549 **Figure 7:** Scatter density plots between AERONET AOD and the predicted AOD (VIS_AOD) and
 550 MERRA-2 AOD before/after 2000 on the monthly scale. The solid black line represents the 1:1 line and
 551 the dashed lines represents expected error (EE) envelopes. The sample size (N), correlation coefficient
 552 (R), mean absolute error (MAE), and root mean square error (RMSE) are given. ‘= EE’, ‘> EE’, and ‘<
 553 EE’ represent the percentages (%) of retrievals falling within, above, and below the EE, respectively.

554 3.3.2 Validation over regions

555 Aerosol loading exhibits spatial variability. Evaluation metrics for the relationships between
 556 visibility-derived AOD and AERONET AOD and Terra AOD for each region are listed in Table 1.

557 In Europe and North America, the results are similar to those of Terra and AERONET, with a large
 558 number of data pairs, greater than 10^5 (AERONET) and greater than 10^7 except for Eastern Europe
 559 (Terra) on the daily scale. Approximately 63% -70% data pairs fall within the EE envelopes. The
 560 RMSE is approximately 0.11, except for western North America (~ 0.15), and the MAE is
 561 approximately 0.07, and the correlation coefficient is between 0.44 and 0.54.

562 In Central South America, South Africa, and Australia, data pairs are about 10^{3-4} (AERONET) and
 563 10^6 (Terra) on the daily scale. 52-60% fall within the EE envelopes compared to AERONET, and
 564 58-67% compared to Terra. The RMSE is 0.03-0.05 compared to Terra, and 0.11-0.17 compared to
 565 AERONET. The correlation coefficient ranges from 0.40 to 0.74, with the highest correlation
 566 coefficient in South America at 0.74.

567 In Asia, India, and West Africa, the data pairs are only approximately 10^4 (AERONET). 32% to 50%
568 fall within the EE envelopes compared to AERONET, the RMSE value ranges from 0.20 to 0.50,
569 and the MAE ranges from 0.11 to 0.36. Compared to Terra AOD, 51 to 58% of data pairs fall within
570 the EE envelopes, the RMSE is around 0.16, and the MAE is around 0.11. Compared to AERONET,
571 in these high aerosol loading regions, RMSE and MAE increase, and the percentages falling within
572 the EE envelopes decrease, but the correlation coefficients do not significantly decrease.

573 Compared to Terra AOD, 55% -67% of data falls within the EE envelopes on the daily scale, 87% -
574 96% on the monthly scale, and over 97% on the yearly scale. Compared to AERONET AOD, 32-
575 68% of data falls within the EE envelopes, 24% -84% on the monthly scale, and 15% -97% on the
576 yearly scale. On both monthly and yearly scales, all metrics have shown a significant increase in
577 performance when compared to Terra. However, compared to AERONET, not all metrics increase
578 in some regions due to limited data pairs, such as West Africa, Northeast Asia, and India, which may
579 be due to the spatial differences between AERONET sites and meteorological stations.

580 **3.3.3 Validation at a site scale**

581 Sites, especially AERONET, are not completely uniform across the world or in any region, and
582 different stations have different sample sizes, which may lead to a certain uncertainty. Therefore,
583 further analysis is conducted on the spatial distribution of different evaluation metrics. Figure 8
584 shows the validation and comparison of daily VIS_AOD against Terra and AERONET AOD at a
585 site scale.

586 Compared to Terra daily AOD, the R of 67% stations is greater than 0.40, the mean bias of 83% is

Table 1: Evaluation metrics for the relationships between visibility-derived AOD and AERONET AOD and Terra AOD for each region.

Region		N			R			RMSE			MAE			Within EE (%)		
		daily	monthly	yearly	daily	monthly	yearly	daily	monthly	yearly	daily	monthly	yearly	daily	monthly	yearly
Eastern Europe	AERONET	21724	2317	271	0.463	0.493	0.653	0.1069	0.0647	0.0326	0.0714	0.0442	0.0263	65.69	83.77	97.42
	TERRA	661630	36435	3278	0.464	0.665	0.790	0.1095	0.0471	0.0214	0.0726	0.0286	0.0122	66.07	94.71	99.18
Western Europe	AERONET	53043	6033	697	0.445	0.487	0.344	0.1089	0.0716	0.0513	0.0711	0.0474	0.0347	64.40	79.21	89.10
	TERRA	1778013	104620	9166	0.467	0.763	0.811	0.1096	0.0391	0.0210	0.0712	0.0268	0.0124	66.99	95.42	99.40
Western North America	AERONET	33859	2948	334	0.503	0.484	0.509	0.1465	0.0949	0.0566	0.0747	0.0597	0.0419	63.58	67.37	81.14
	TERRA	1725226	82734	7201	0.542	0.765	0.906	0.1144	0.0465	0.0180	0.0671	0.0267	0.0125	69.48	94.42	99.61
Eastern North America	AERONET	47407	5359	608	0.527	0.526	0.559	0.1135	0.0824	0.0436	0.0657	0.0472	0.0331	67.52	77.78	87.50
	TERRA	6280277	359520	31343	0.515	0.799	0.847	0.1159	0.0435	0.0165	0.0726	0.0275	0.0111	66.70	94.94	99.80
Central South America	AERONET	10911	1176	149	0.740	0.811	0.866	0.1735	0.1272	0.1060	0.1021	0.0904	0.0688	52.40	47.96	67.79
	TERRA	444780	26362	2410	0.545	0.820	0.776	0.1447	0.0591	0.0369	0.0909	0.0396	0.0219	58.48	89.29	97.39
Southern Africa	AERONET	4255	309	38	0.423	0.480	0.630	0.1553	0.1128	0.0705	0.1033	0.0805	0.0525	52.08	59.55	78.95
	TERRA	216239	11304	1118	0.518	0.821	0.870	0.1258	0.0511	0.0296	0.0836	0.0340	0.0191	60.64	91.70	98.21
Australia	AERONET	6426	516	63	0.488	0.654	0.363	0.1094	0.0827	0.0725	0.0711	0.0620	0.0563	59.96	59.88	71.43
	TERRA	284693	14588	1286	0.398	0.784	0.831	0.1091	0.0363	0.0188	0.0666	0.0261	0.0143	67.01	94.65	99.38
Western Africa	AERONET	2205	205	34	0.553	0.594	0.762	0.3180	0.2873	0.3357	0.2082	0.2029	0.2587	37.96	40.00	23.53
	TERRA	156392	10468	1028	0.501	0.769	0.849	0.1769	0.0706	0.0412	0.1198	0.0482	0.0242	51.83	88.01	97.57
Southeast Asia	AERONET	4134	504	74	0.405	0.542	0.488	0.2037	0.1447	0.1198	0.1274	0.0988	0.0821	50.17	56.15	60.81
	TERRA	402465	27058	2500	0.470	0.753	0.872	0.1730	0.0729	0.0342	0.109	0.0455	0.0198	57.25	87.01	97.96
Eastern China	AERONET	7396	927	118	0.513	0.551	0.356	0.3571	0.2355	0.1933	0.2038	0.1392	0.1382	40.10	49.84	50.00
	TERRA	241185	17324	1518	0.523	0.811	0.895	0.1646	0.0638	0.0302	0.1073	0.0435	0.0225	55.77	88.07	98.88
Northeast Asia	AERONET	9979	1178	142	0.569	0.593	0.367	0.4941	0.3249	0.2604	0.2924	0.2425	0.2202	35.17	29.54	21.13
	TERRA	78823	5485	467	0.553	0.872	0.965	0.1973	0.0636	0.0263	0.1201	0.0440	0.0198	56.48	87.77	98.29

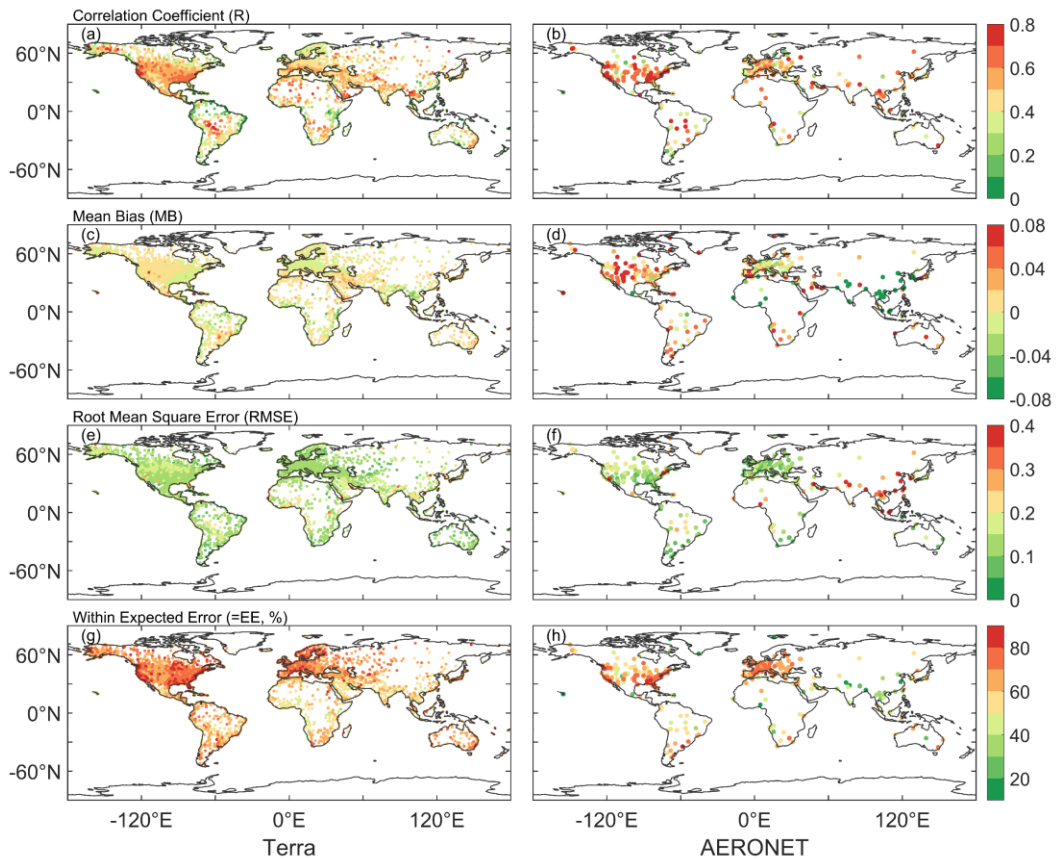
<i>India</i>	<i>AERONET</i>	2208	203	32	0.521	0.462	0.534	0.2957	0.3015	0.3588	0.2049	0.2283	0.2862	32.11	24.63	15.63
	<i>TERRA</i>	179928	9564	862	0.526	0.815	0.915	0.1564	0.0599	0.0352	0.1089	0.042	0.0238	55.16	90.43	98.14

588

589 less than 0.01, the RMSE of 85% is less than 0.15, and the percentage falling within the EE of 67%
590 is greater than 60%. More than 85% of stations falling within the EE is greater than 60% in Europe,
591 North America, and Oceania, while 40-60% in South America, Africa, and Asia. The percentage of
592 expected error is low in South and East Asia, and Central Africa, with some underestimation. Above
593 60% in Africa, Asia, North America, and Europe have a correlation coefficient greater than 0.40.
594 The regions with lower correlation are the coastal regions of South America, eastern Africa, western
595 Australia, northeastern North America, and northern Europe. Above 90% of the RMSE in Europe,
596 North America, and Oceania are smaller than 0.15. High RMSE regions are in western North
597 America, Asia, central South America, and central Africa.

598 Compared to AERONET daily AOD, the R of 74% stations is greater than 0.40, and the spatial
599 distribution is similar to Terra's. The mean bias of 44% is less than 0.01, the RMSE of 68% is less
600 than 0.15, and the percentage falling within the EE of 53% is greater than 60%. More than 70% of
601 sites have a correlation coefficient greater than 0.40 in Africa, Asia, Europe, and North America.
602 More than 57% of sites have an expected error percentage of over 60% in Europe, North America,
603 and Oceania, except for Asia. Over 72% of sites have a RMSE less than 0.15. Except for Oceania
604 and South America, over 71% of sites in other regions have MAEs less than 0.01. Almost all sites
605 in Asia show a negative bias, significantly underestimating. However, there is a significant
606 overestimation in western North America and western Australia. Most sites in Asia falling within
607 the expected error are less than 50%. High RMSE are in high emission and dust areas, such as Asia,
608 India, and Africa.

609 The validation and comparison on the site scale show a limitation similar to the MODIS DT
610 algorithm. In areas with high vegetation coverage, the AOD from visibility are better than those in
611 bright areas. Although the correlation coefficients are high in high aerosol loading areas (Central
612 South America, West Africa, India, Eastern China, Northeast Asia), there are significant differences
613 in these areas with high RMSE values. As shown in Figure 6, some stations located in dusty and
614 urban areas are overestimated or underestimated. Studies have shown that there is a significant
615 uncertainty in the MODIS retrievals in these regions, and the challenges of inversion algorithms are
616 significant in bright surfaces (desert and snow covered areas) and urban surface of densely
617 populated complex structures (Chu et al., 2002; Remer et al., 2005; Levy et al., 2010; Wei et al.,
618 2019; Wei et al., 2020). In India, the elevation difference between AERONET site and
619 meteorological station reached 0.7 km may be a factor affecting the validation effect, as aerosol
620 varies greatly with altitude. In eastern China, the complex urban surface, emission sources, and
621 observations in different locations (AERONET site and meteorological station) may be the reasons
622 for underestimation. At the same time, visibility stations in desert areas are sparse, and the spatial
623 variability of dust aerosols is large, which also increases the difficulty to estimate VIS_AOD.



624

625 **Figure 8:** Validation of VIS_AOD against Terra and AERONET AODs at each site: (a–b)
 626 correlation (R), (c–d) mean bias (MB), (e–f) root mean square error (RMSE), (g–h) percentage (%)
 627 of VIS_AOD within the expected error envelopes.

628 3.3.4 Discussion and uncertainty analysis

629 The atmospheric visibility is a surface physical quantity, while AOD is a column-integrated physical
 630 quantity. We have linked the two variables together using machine a learning method, which
 631 partially compensates for the scarcity of AOD data. However, we have to face some limitations.
 632 Although the boundary layer height is considered, it is not sufficient. Pollutants such as smoke from
 633 biomass burning, dust, volcanic ash, and gas-aerosol conversion of sulfur dioxide to sulfate aerosols
 634 in the upper and lower troposphere can undergo long-range aerosol transport under the influence of
 635 circulation. The pollution transport and aerosol conversion processes above the boundary layer are
 636 still significant and cannot be ignored (Eck et al., 2023). Compared to surface visibility, bias occurs
 637 when the aerosol layer rises and affects AERONET measurements and MODIS retrievals. Therefore,
 638 it should be considered when using this data. If there are sufficient historical vertical aerosol
 639 measurements with high temporal and spatial resolution, the results of this data would be greatly
 640 improved. Although some studies use aerosol profiles from pollution transport models or assumed
 641 profiles as substitutes for observed profiles (Li et al., 2020; Zhang et al., 2020), the biases introduced
 642 by these non-observed profiles are still significant.

643 In machine learning, we use MODIS Aqua AOD as the target value for the model because the
 644 validation results for MODIS C6.1 product have a correlation coefficient of 0.9 or higher with
 645 AERONET AOD on the daily scale (Wei et al., 2019; Wei et al., 2020). Compared to AERONET,

646 MODIS AOD provides more sample data with a high global coverage. However, apart from
647 modeling errors, the systematic biases and uncertainties of MODIS Aqua AOD cannot be ignored
648 (Levy et al., 2013; Levy et al., 2018; Wei et al., 2019). Averaging over time scale can reduce
649 representation errors effectively, and emission sources and orography can increase representation
650 errors (Schutgens et al., 2017). Therefore, the strong correlation at monthly and annual scales
651 indicates a substantial reduction in errors. This is also one of the reasons why this dataset shows
652 stronger correlation with Terra AOD and weaker correlation with AERONET in validation.

653 The spatial matching between meteorological stations and AERONET sites may cause some biases.
654 AERONET sites are usually not co-located with meteorological stations in terms of elevation and
655 horizontal distance, this is another reason for the weak correlation between VIS_AOD and
656 AERONET AOD. The meteorological stations are located at the airport. Different horizontal
657 distances may result in meteorological stations and AERONET sites being located on different
658 surfaces (such as urban, forest, mountainous). Differences in site elevation significantly impact the
659 relationship between AOD and measured visibility. When the AERONET site is at a higher elevation
660 than the meteorological station, there may be fewer measurements of aerosols over the sea at the
661 AERONET site.

662 Different pollution levels and station elevation affect the AOD derived from visibility. The elevation
663 difference and distance between meteorological stations and AERONET sites also have an impact
664 on the validation results. Therefore, the error and performance of different AERONET AOD values,
665 station elevation, and distance are analyzed.

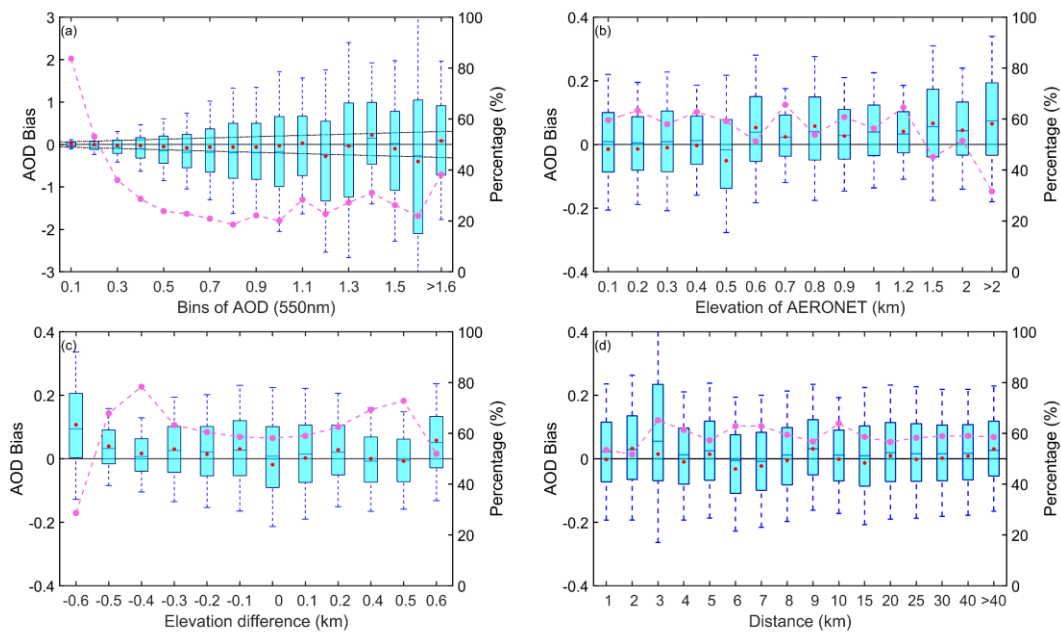
666 As the AOD increases, the variability of bias also increases in Figure 9 (a). Almost all mean bias
667 values are within the envelope of EE, except for 1.1-1.2 and 1.5-1.6. The average bias is 0.015
668 (AOD < 0.1), with 83% of data within the EE envelopes. The mean bias is -0.0011 (AOD, 0.1-0.2),
669 with 54% within the EE envelopes. The mean bias is negative (AOD, 0.3-1.0), with 20%-40%
670 falling within the EE envelopes. There is a positive bias (AOD, 1.1, 1.4 and > 1.6), and there is a
671 negative bias at 1.2-1.3 and 1.5-1.6. The results indicate that as pollution level increases, the
672 negative mean bias becomes significant and the underestimation increases.

673 The contribution of aerosols near the ground to the column aerosol loading is significant. The
674 elevation of the site affects the measurement of column aerosol loading in Figure 9 (b). There is a
675 negative bias in the low elevation (≤ 0.5 km) with a percentage of 60%-64% falling within the EE
676 envelopes and a positive bias in high elevation (0.5-1.2 km) with a percentage of 50%-65% falling
677 within the EE envelopes. The percentage significantly decreases (> 1.2 km), and the average bias
678 increases. Therefore, the elevation of AERONET's site will cause bias in validation, and the
679 uncertainty greatly increases in high elevation.

680 Due to the elevation difference between the meteorological station and AERONET site in the
681 vertical direction, the uncertainty caused by elevation differences of site is analyzed in Figure 9 (c).
682 When the elevation difference is negative (the elevation of the meteorological station is lower than
683 that of the AERONET station), there is a significant positive bias. When the difference is positive,
684 the mean bias approaches 0 or is positive. The percentage is greater than 60% (-0.5 km-0.5 km).
685 The positive mean bias is greater than the negative mean bias, and the uncertainty greatly increases
686 when the elevation of meteorological stations is lower than that of AERONET sites. It indicates that
687 the contribution of the near surface aerosol to the column aerosol loading is significant and cannot

688 be ignored.

689 The spatial variability of aerosols is significant. Meteorological stations and AERONET sites are
690 not collocated, resulting in a certain distance in spatial matching. In this study, the upper limit of
691 distance is 0.5 degree. Figure 9 (d) shows the error of the distance between stations, where the
692 degree is converted to the distance at WGS84 coordinates. The bias does not change significantly
693 with increasing distance. The average bias is around 0, with the maximum positive mean bias
694 (0.0322) at a distance of 2 km and the maximum negative mean deviation (-0.0323) at 6 km. The
695 median is almost positive, except at 5 km and 6 km. The percentage falling within the EE envelopes
696 is over 50%, with the maximum percentage (66%) at 3km and the minimum (62%) at 2 km.



697

698 **Figure 9:** Box plots of AOD bias and the percentage falling within the EE envelopes (curves): (a)
699 AERONET AOD levels, (b) elevation of AERONET sites, (c) elevation difference between
700 meteorological stations and AERONET sites, (d) distance (km) between meteorological stations and
701 AERONET sites. The black horizontal line represents the zero bias. For each box, the upper, lower,
702 and middle horizontal lines, and whiskers represent the AOD bias 75th and 25th percentiles, median,
703 and 1.5 times the interquartile difference, respectively. The black solid lines represent the EE
704 envelopes ($\pm (0.05 + 0.15 * AOD_{AERONET})$). No site with a difference of + 0.3 km (x-axis label
705 without 0.3) in (c).

706 3.4 Interannual variability and trend of visibility-derived AOD over global land

707 The multi-year average AOD from 1980 to 2021 over land is 0.177, as shown in Figure 10 (a). The
708 average is 0.178 in Northern Hemisphere (NH, 4532 stations) and 0.174 in Southern Hemispheres
709 (SH, 500 stations). Due to the influence of geography, atmospheric circulation, population, and
710 emissions, the AOD varies in different latitudes. Figure 11 illustrates the multi-year average AOD
711 in different latitude ranges from 1980 to 2021. The AOD value in the NH is higher than that over
712 land, then higher than that in the SH. Within [-20, 20°N], the average AOD reaches its maximum
713 (0.225), and the maximum AOD in the NH is 0.239 in [0, 20°N]. The highest AOD in the SH is

714 0.203 in in [-15, 0°N]. The average AOD rapidly decreases from -15°N to -35°N in the SH and from
715 20°N to 50°N in the NH.

716 There are many regions of high AOD values occur in the NH, with the distribution of high
717 population density. Approximately 7/8 of the global population resides in the NH, with 50%
718 concentrated at 20°N-40°N (Kummu et al., 2016), indicating a significant impact of human activities
719 on aerosols. The highest AOD values are observed near 17°N, including the Sahara Desert, Arabian
720 Peninsula, and India, suggesting that in addition to anthropogenic sources, deserts also play a crucial
721 role in aerosol emissions. Lower AOD regions of the SH are from 25°S to 60°S, encompassing
722 Australia, southern Africa, and southern South America, indicating lower aerosol burdens in these
723 areas. Additionally, North America also exhibits low aerosol loading. Chin et al. (2014) analyzed
724 the AOD over land from 1980 to 2009 with the Goddard Chemistry Aerosol Radiation and Transport
725 model, which is similar to the visibility-derived AOD. The spatial distribution is consistent with the
726 satellite results (Remer et al., 2008; Hsu et al., 2012; Hsu et al., 2017; Tian et al., 2023). The AOD
727 and extinction coefficient retrieved from visibility show a similar distribution at global scale, with
728 a correlation coefficient of nearly 0.6 (Mahowald et al., 2007). Similar global (Husar et al., 2000;
729 Wang et al., 2009) and regional (Koelemeijer et al., 2006; Wu et al., 2014; Boers et al., 2015; Zhang
730 et al., 2017; Zhang et al., 2020) spatial distributions have been reported.

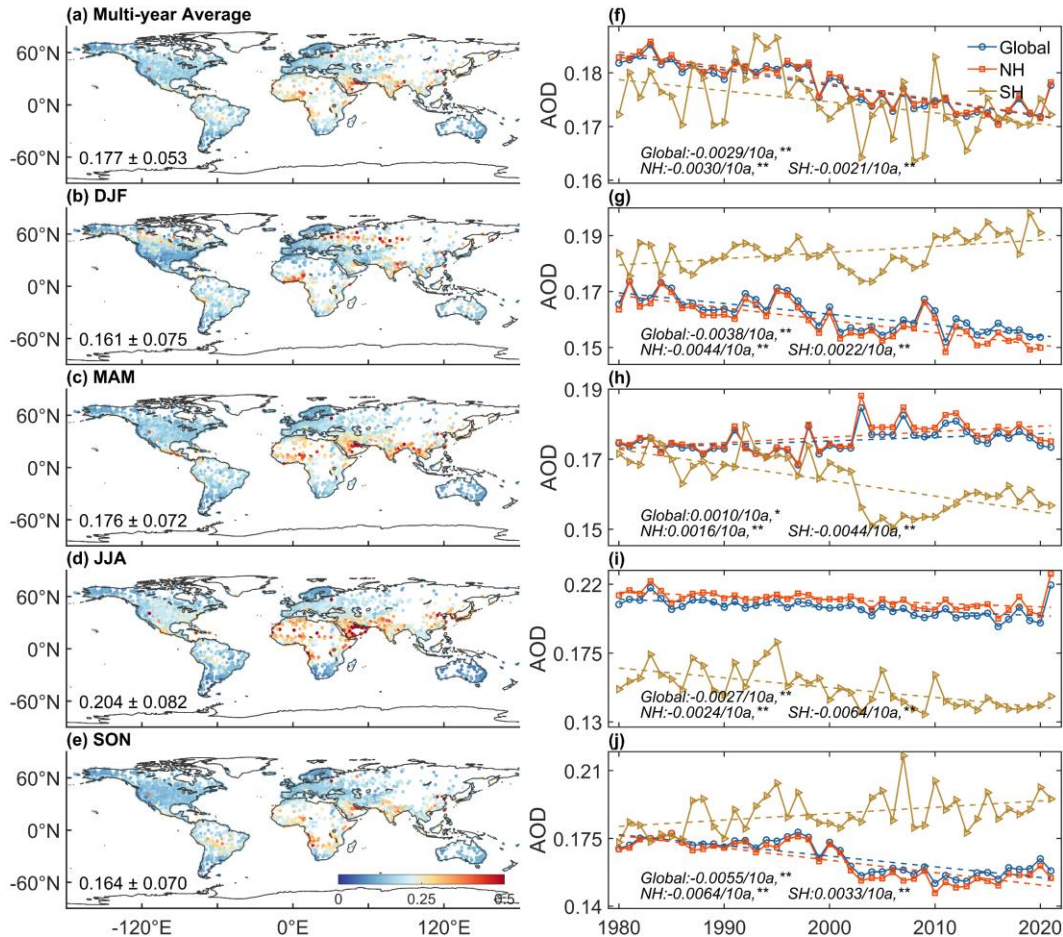
731 AOD loadings exhibit significant seasonal variations worldwide, particularly over land. In this study,
732 a year is divided into four parts: December-January-February (DJF), March-April-May (MAM),
733 June-July-August (JJA), and September-October-November (SON), corresponding to winter
734 (summer), spring (autumn), summer (winter), and autumn (spring) in the NH (SH), respectively.
735 Figure 10 (b-e) also depicts the spatial distribution of seasonal average AOD over land from 1980
736 to 2021. The global AOD in DJF, MAM, JJA, and SON is 0.161, 0.176, 0.204, and 0.164,
737 respectively. The standard bias of AOD in JJA and DJF are greater than those in DJF and SON.
738 AOD exhibits seasonal changes, with the highest in JJA, followed by DJF, MAM and SON.

739 In the NH, the AOD ranking is summer (0.210) > spring (0.176) > autumn (0.163) > winter (0.160).
740 In the SH, the AOD ranking from high to low in season is spring (0.188) > summer (0.184) > autumn
741 (0.164) > winter (0.152). The highest AOD is observed during JJA in the NH, while in the SH, the
742 peak occurs during SON. The high AOD value is highly associated with the growth of hygroscopic
743 particle and the photochemical reaction of aerosol precursors under higher relative humidity in Asia
744 (JJA) (Remer et al., 2008) and Europe such as Russia (JJA), and biomass burning in South America
745 (SON), Southern Africa (SON), and Indonesia (SON) (Ivanova et al., 2010; Krylov et al., 2014). On
746 the other hand, the lowest global AOD values are observed during winter, which may be attributed
747 to the atmospheric circulation systems (Li et al., 2016; Zhao et al., 2019).

748 The temporal variations in AOD have also been of great interest due to the significant relationship
749 between aerosols and climate change. Figure 10 (f) shows the trends of annual average AOD (**
750 represents passing the significance test, $p < 0.01$) over the global land, the SH and the NH during
751 1980-2021. The global land, NH, and SH trends demonstrate decreasing trends of AOD with values
752 of -0.0029/10a, -0.0030/10a, and -0.0021/10a, respectively, with all passing the significance test.
753 The declining trend is much greater in the NH than in the SH.

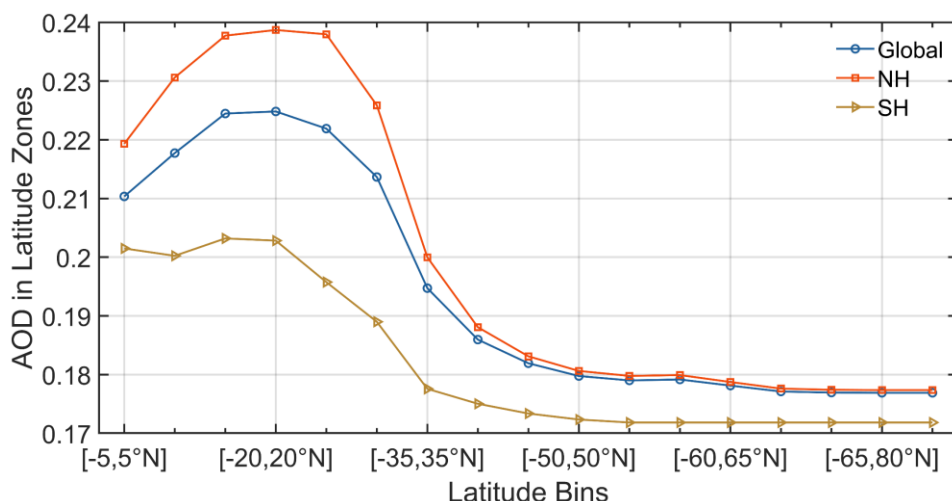
754 The seasonal trends of AOD during 1980-2021 at the global and hemispheric scales are shown in
755 Figure 10 (g-j). The trend over land is decreasing in DJF, JJA and SON, and increasing in MAM.

756 The largest declining trend is observed in SON ($-0.0055/10a$). In the NH, the trends are $-0.0044/10a$
 757 (DJF), $0.0016/10a$ (MAM), $-0.0024/10a$ (JJA), and $-0.0064/10a$ (SON). In the SH, the trends are as
 758 follows: $0.0022/10a$ (DJF), $-0.0044/10a$ (MAM), $-0.0064/10a$ (JJA), and $0.0033/10a$ (SON). The
 759 largest declining trend is SON in the NH and JJA in the SH. However, the trends are positive in
 760 MAM of the NH and DJF and SON of the SH.



761

762 **Figure 10:** The map of annual and seasonal mean AOD (left) and global/regional mean time series
 763 from 1980 to 2021 (right). Global land (circle), northern hemisphere (NH) (triangle) and southern
 764 hemisphere (SH) (square) annual and seasonal AOD. The symbol, **, represents that the trend
 765 passed the test at a significance level of 0.01. The symbol, *, represents that the trend passed the
 766 test at a significance level of 0.05. DJF represents December and next January and February. MAM
 767 represents March, April, and May. JJA represents June, July, and August. SON represents September,
 768 October, and November.



769

770 **Figure 11:** The global land (blue), northern hemisphere's (red) and southern hemisphere's (yellow)
 771 multi-year average VIS_AOD from 1980 to 2021 in different latitude zones. The latitude range is
 772 from -65 to 85°N, with a bin of 5°.

773 3.5 Interannual variability and trend of visibility-derived AOD over regions

774 The distribution of AOD over global land exhibits significant spatial heterogeneity. Large variations
 775 in aerosol concentrations exist among different regions, leading to a non-uniform spatial distribution
 776 of AOD globally. Accurately assessing the long-term trends of aerosol loading is a key for
 777 quantifying aerosol climate change, and it is crucial for evaluating the effectiveness of
 778 measurements implemented to improve regional air quality and reduce anthropogenic aerosol
 779 emissions. Therefore, we select 12 representative regions to analyze the variability and trend of
 780 AOD, which are influenced by various aerosol sources (Wang et al., 2009; Hsu et al., 2012; Chin et
 781 al., 2014), such as desert, industry, anthropogenic emissions, and biomass burning emissions, which
 782 nearly cover the most land and are densely populated regions (Kummu et al., 2016). These
 783 representative regions are Eastern Europe, Western Europe, Western North America, Eastern North
 784 America, Central South America, Western Africa, Southern Africa, Australia, Southeast Asia,
 785 Northeast Asia, Eastern China, and India, as shown in Figure 1.

786 The multi-year average and seasonal average AOD (Figure 12), the trends of the annual average of
 787 monthly anomalies (Figure 13), and the seasonal trends (Figure 14) are analyzed in 12 regions from
 788 1980 to 2021.

789 The regions with a high aerosol level ($AOD > 0.2$) are in West Africa, Southeast and Northeast Asia,
 790 Eastern China, and India. The AOD values range from 0.15 to 0.2 in Eastern Europe, Western
 791 Europe, Eastern North America, Central South America, and South Africa. The AOD values are less
 792 than 0.15 in Western North America and Australia.

793 Europe is an industrial region with a low aerosol loading region, and the multi-year average AOD
 794 in Eastern Europe (0.181) is higher than that in Western Europe (0.163) during 1980-2021. Eastern
 795 Europe shows a greater downward trend in AOD (-0.0067/10a) compared to Western Europe (-
 796 0.0026/10a). The highest AOD is observed in JJA, the dry period when solar irradiation and
 797 boundary layer height increase, with AOD values of 0.201 in Eastern Europe and 0.162 in Western

798 Europe, which could be due to increases in secondary aerosols, biomass burning, and dust transport
799 from the Sahara (Mehta et al., 2016). However, there are seasonal variations. In Eastern Europe, the
800 seasonal AOD ranking from high to low is JJA (0.201) > DJF (0.181) > MAM (0.175) > SON
801 (0.161), while in Western Europe, it is JJA (0.193) > MAM (0.162) > SON (0.160) > DJF (0.138).
802 The differences among seasons are larger in Western Europe. AOD in Eastern Europe shows
803 declining trends ($p < 0.01$) in all seasons, and the largest declining trend is in DJF (-0.0096/10a). In
804 Western Europe, the AOD in DJF, JJA, and SON exhibits declining trends, while the AOD in MAM
805 shows a significant increasing trend (0.0019/10a). The trends in both Western and Eastern Europe
806 are increasing in MAM from 1995 to 2005 with Western Europe showing a greater increasing trend.
807 However, after 2005, the decline rates accelerate in each season. Studies have shown the downward
808 trend in Europe is attributed to the reduction of biomass burning, anthropogenic aerosols, and
809 aerosol precursors (such as sulfur dioxide) (Wang et al., 2009; Chin et al., 2014; Mortier et al., 2020).

810 North America is also an industrial region with a low aerosol loading. The average AOD values in
811 Eastern and Western North America during 1980-2021 are 0.165 and 0.146, respectively, with the
812 Eastern region being higher than the Western region by 0.019. From 1980 to 2021, both Eastern (-
813 0.0027/10a) and Western North America (-0.0017/10a) show a downward trend. The AOD values
814 in DJF, MAM, JJA, and SON in Western North America are 0.141, 0.148, 0.163, and 0.130,
815 respectively, and 0.138, 0.156, 0.216, and 0.149 in Eastern North America. Specifically, the trends
816 of the Western and Eastern region are increasing during MAM and decreasing during other seasons.
817 In the Western region, the trend is increasing after 2005, while in the Eastern region, there is no
818 increasing trend. The increasing trend may be due to low rainfall and increased wildfire activities
819 (Yoon et al., 2014). The decrease in Eastern North America is related to the reduction of sulfate and
820 organic aerosols, as well as the decrease in anthropogenic emissions caused by environmental
821 regulations (Mehta et al., 2016).

822 Central South America is a relatively high aerosol loading region, sourced from biomass burning,
823 especially in SON (Remer et al., 2008; Mehta et al., 2016), with a multi-year average AOD of 0.198.
824 There is a downward trend (-0.0075/10a) from 1980 to 2021. The trend is slightly lower than the
825 trend (-0.0090/10a) from 1998 to 2010 (Hsu et al., 2012) and the trend is decreasing from 1980 to
826 2006 (Streets et al., 2009) and from 2001 to 2014 (Mehta et al., 2016). The AOD values in DJF
827 (0.207) and SON (0.228) are higher compared to the values in MAM (0.185) and JJA (0.171), and
828 the larger declining trends are observed in MAM (-0.0100/10a) and JJA (-0.0150/10a). The result
829 indicates that although AOD has decreased overall, the aerosol loading is still high, which is caused
830 by deforestation and biomass burning (Mehta et al., 2016).

831 Africa is a high aerosol loading region worldwide. In West Africa, the multi-year average AOD is
832 0.281, and the trend is decreasing (-0.0062/10a) from 1980 to 2021. The world's largest desert
833 (Sahara Desert) is in West Africa, with much dust emission. The AOD values in JJA (0.296), MAM
834 (0.292), DJF (0.276) and SON (0.261) are above 0.26. The trends in DJF (-0.0145/10a), MAM (-
835 0.0015/10a), JJA (-0.0019/10a) and SON (-0.0078/10) are decreasing. For South Africa, the multi-
836 year average AOD is 0.182, lower than that of West Africa. The trend is decreasing (-0.0016/10a).
837 The results of AERONET observations and simulation also show a decreasing trend (Chin et al.,
838 2014). The AOD values range from 0.12 to 0.20 during 2000-2009, dominated by fine particle
839 matter from industrial pollution from biomass and fossil fuel combustion (Hersey et al., 2015). The

840 average AOD values in DJF, MAM, JJA, and SON are 0.207, 0.173, 0.135, and 0.21, with trends of
841 0.0044/10a, -0.0089/10a, -0.0089/10a and 0.0063/10a, respectively.

842 Australia is a region with a low aerosol loading. The multi-year average AOD is 0.133 during 1980-
843 2021. The AOD ranges from 0.05 to 0.15 from AERONET during 2000-2021, and dust and biomass
844 burning are important contributors to the aerosol loading (Yang et al., 2021a). There is a downward
845 trend of AOD (-0.0028/10a), which may be related to a decrease in dust and biomass burning (Yoon
846 et al., 2016; Yang et al., 2021a). In addition, a research has shown that the forest area in Australia
847 has increased sharply since 2000 (Giglio et al., 2013), surpassing the forest fire area of the past 14
848 years. The seasonal average of AOD in MAM, JJA, SON, and DJF are 0.130, 0.107, 0.132, and
849 0.161. The AOD in JJA is the lowest in all seasons and in all regions. The trends in DJF and SON
850 are increasing, and the trends in MAM and JJA are decreasing. Ground-based observations and
851 satellite retrievals indicate that wildfires, biomass burning and sandstorms lead to high AOD in DJF
852 and SON. The low AOD of MAM and JJA is due to a decrease in the frequency of sandstorms and
853 wildfires and an increase in precipitation (Gras et al., 1999; Yang et al., 2021a; Yang et al., 2021b).

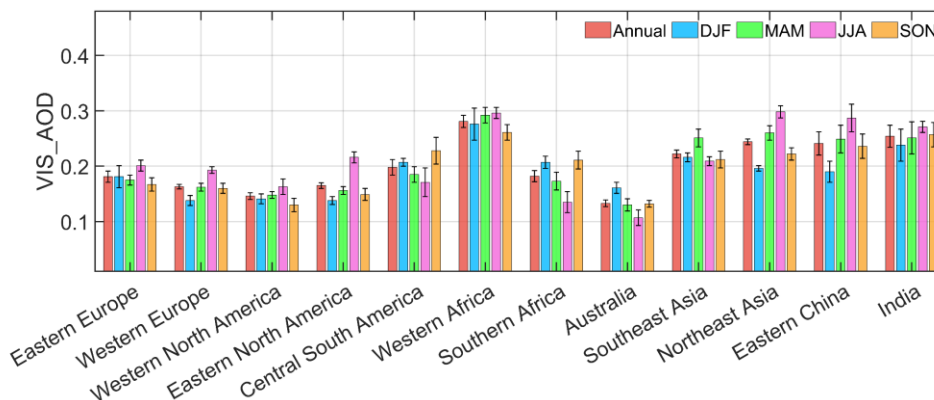
854 Asia is also a high aerosol loading area with various sources. In Southeast Asia, the multi-year
855 average AOD is 0.222 during 1980-2021 with a downward trend of AOD (0.0007/10a). It is also a
856 biomass-burning area. The seasonal average AOD ranking is MAM (0.251) > DJF (0.216) > SON
857 (0.212) > JJA (0.209). The trend in DJF (-0.0018/10a) is decreasing and the trends in MAM
858 (0.033/10a), JJA (0.0008/10a) and SON (0.0006/10a) are increasing. However, the trends are
859 insignificant. Southeast Asia has no clear long-term trend in the estimated AOD or ground-based
860 observations (Streets et al., 2009). In Northeast Asia, the multi-year average AOD is 0.244 during
861 1980-2021, with a trend of -0.0009/10a. The trend is increasing (0.0018/10a) during 1980-2014 and
862 decreasing (-0.0213/10a) during 2014-2021. The seasonal AOD values are 0.196 in DJF, 0.260 in
863 MAM, 0.287 in JJA and 0.236 in SON. The high aerosol level is related to dust and aerosol
864 transportation in East Asia. The trends in DJF (0.0016/10a), MAM (0.0062/10a) are increasing, and
865 the trends in JJA (-0.0043/10a) and SON (-0.0070/10a) are decreasing. In Eastern China, the multi-
866 year average AOD is 0.241, with an increasing trend (0.0130/10a). The trend is 0.0196/10a from
867 1980 to 2014 and -0.0572/10a from 2014 to 2021. The seasonal ranking of AOD from high to low is
868 JJA (0.287), MAM (0.249), SON (0.236) and DJF (0.216). The AOD trends in DJF (0.0133/10a),
869 MAM (0.0179/10a), JJA (0.0107/10a) and SON (0.0105/10a) are all positive. The trend can be
870 divided into three stages: 1980-2005, 2006-2013 and 2014-2021. In the first stage, AOD values are
871 increasing steadily. In the second stage, AOD values maintain a high level. In the third stage, the
872 AOD values experience a rapid decline, reaching the level in 1980s by 2021. The increasing trend
873 of AOD before 2006 may be due to the significant increase in industrial activity, and after 2013, the
874 significant decrease is closely related to the implementation of air quality-related laws and
875 regulations, along with adjustments in the energy structure (Hu et al., 2018; Cherian and Quaas,
876 2020).

877 India is a high aerosol loading area. The multi-year average AOD is 0.254, with an increasing trend
878 (0.0119/10a) from 1980 to 2021. Dust and biomass burning have an influence on AOD. There are
879 three stages: 1980-1997 (0.0050/10a), 1997-2005 (-0.0393/10a), 2005-2021 (0.0446/10a). The
880 seasonal average AOD values are 0.238 in DJF, 0.251 in MAM, 0.271 in JJA, and 0.257 in SON.
881 The largest AOD is in JJA. In winter and autumn, the aerosol level is affected by biomass burning,
882 and in spring and summer, it is also affected by dust, transported from the Sahara under during the

883 monsoon period (Remer et al., 2008). The trends in DJF (0.0186/10a), MAM (0.0143/10a), JJA
884 (0.0012/10a), and SON (0.0129/10a) are positive.

885 The above results have supplemented the existing estimates of long-term AOD variability and trend
886 over land. The AOD level at regional scale is significant differences from 1980 to 2021, which is
887 significantly related to the aerosol emission source types, transportation and the implementation of
888 laws and regulations about pollution control.

889

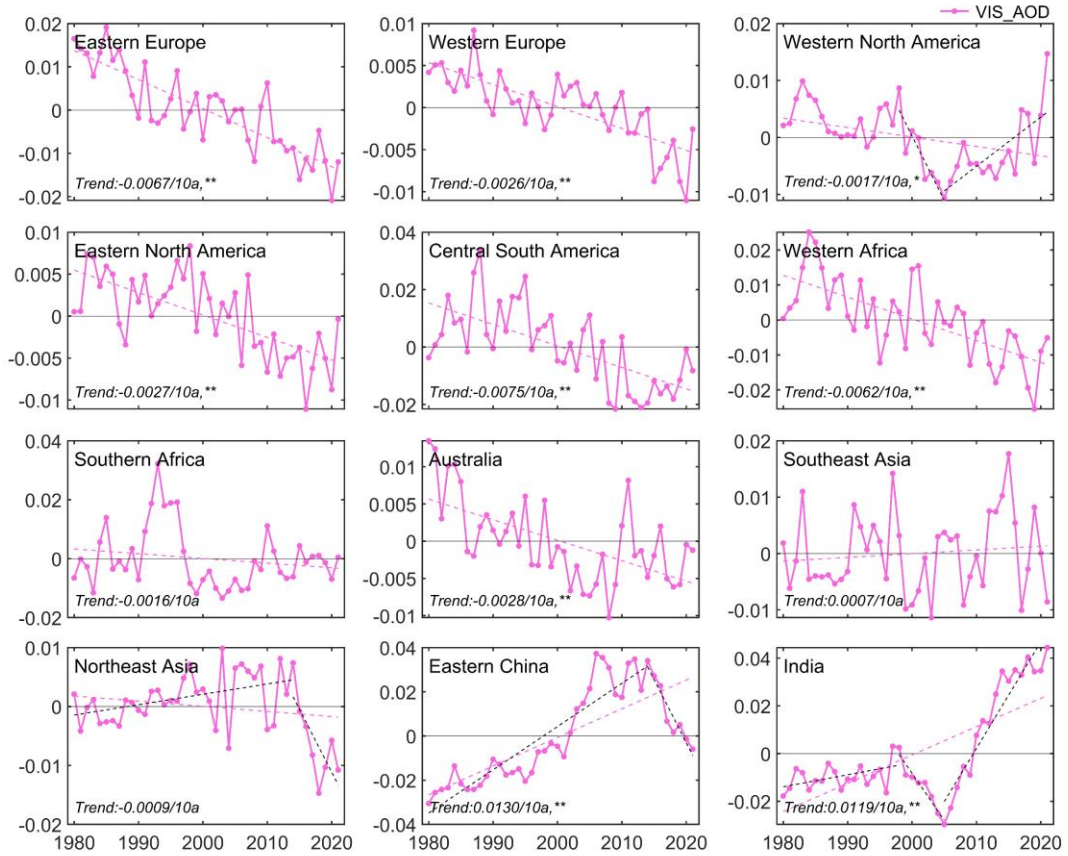


890

891 **Figure 12:** Annual and seasonal mean AOD in 12 regions (Eastern Europe, Western Europe,
892 Western North America, Eastern North America, Central South America, Western Africa, Southern
893 Africa, Australia, Southeast Asia, Northeast Asia, Eastern China, and India) during the period of
894 1980-2021.

895

896

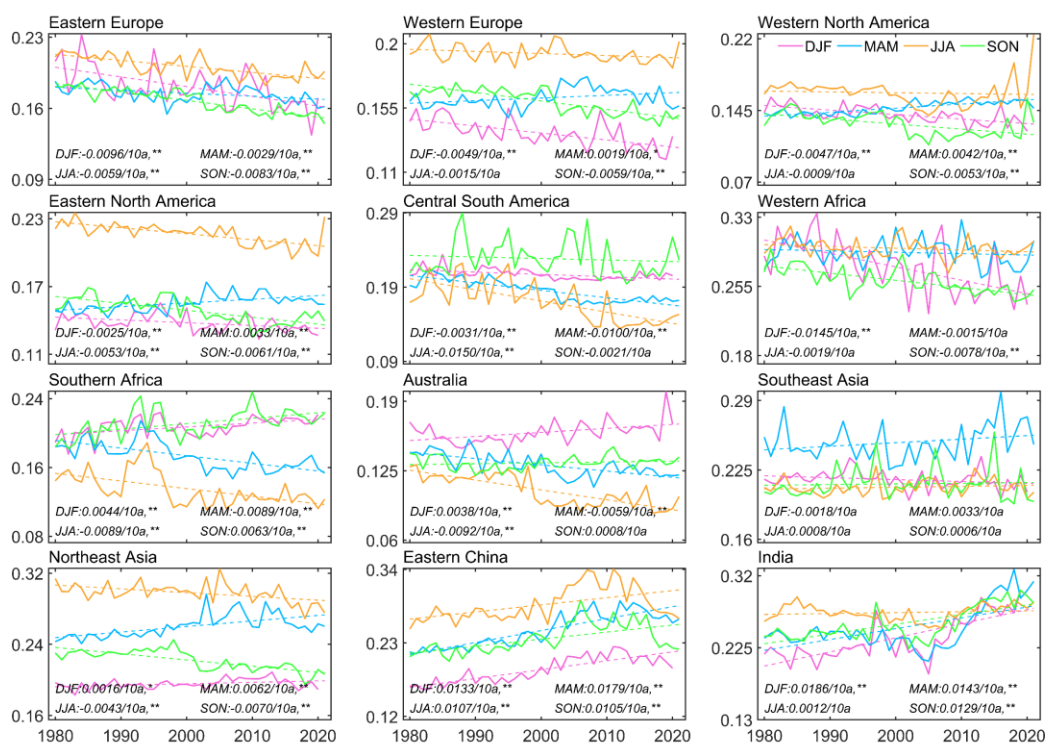


897

898 **Figure 13:** Annual anomaly of VIS_AOD from 1980 to 2021 in 12 regions (Eastern Europe,
 899 Western Europe, Western North America, Eastern North America, Central South America, Western
 900 Africa, Southern Africa, Australia, Southeast Asia, Northeast Asia, Eastern China, and India). The
 901 dotted line is the trend line.

902

903



904

905 **Figure 14:** Seasonal mean VIS_AOD from 1980 to 2021 in 12 regions (Eastern Europe, Western
 906 Europe, Western North America, Eastern North America, Central South America, Western Africa,
 907 Southern Africa, Australia, Southeast Asia, Northeast Asia, Eastern China, and India). The dotted
 908 line is the trend line.

909 4 Data availability

910 We provide the daily visibility-derived AOD data at 5032 stations over global land from 1959-2021,
 911 which is available at National Tibetan Plateau / Third Pole Environment Data Center,
 912 <https://doi.org/10.11888/Atmos.tpcdc.300822> (Hao et al., 2023). Due to a small number and sparse
 913 visibility stations prior to 1980, the global/regional analysis in this study is from 1980 to 2021. The
 914 following is a description to the AOD dataset.

915 The station-scale AOD files are in ‘Station_Daily_AOD_1959_2021.zip’. The station-scale AOD
 916 files can be directly opened by a text program (such as Notepad). The details station information is
 917 in the file of ‘0A0A-Station_ In Information.txt’. There are eight columns in each text file, separated
 918 by commas and the column names are Datetime, TEMP (°C), DEW (°C), RH (%), WS (m/s), SLP
 919 (hPa), DRYVIS (km), and VIS_AOD (550nm). The first column name is the date. The column name,
 920 ‘VIS_AOD (550nm)’, is the AOD at 550 nm. The 2-7th column names are temperature (unit: °C),
 921 dew temperature (unit: °C), relative humidity (unit: %), wind speed (unit: m/s), sea level pressure
 922 (unit: hPa), and dry visibility (unit: km). The more details are in ‘0A0B-ReadMe.txt’.

923 5 Conclusions

924 In this study, we employ a machine learning method to derive daily AOD at 550 nm from 1959 to
925 2021 at 5032 land stations worldwide, based on visibility, satellite retrieval, and related
926 meteorological variables. In the model, Aqua MODIS AOD (550 nm) is set as the target and
927 visibility and related meteorological variables are set as the predictor. The performance and
928 predictive ability of the model are evaluated and validated against AERONET ground-based
929 observations, Terra MODIS AOD and MRRRA-2 AOD. We provide a long-term daily AOD (550
930 nm) dataset at 5032 global land stations from 1959 to 2021. The dataset has complemented the
931 shortcomings of AOD data in terms of time scale and spatial coverage over land. Finally, the
932 variability and trend of AOD are analyzed at global and regional scales in the past 42 years. Several
933 key findings have been given in this study as follows.

934 **1. Modeling evaluation.** For all stations, the mean RMSE, MAE, and R of the model are 0.078,
935 0.044, and 0.75, respectively. The RMSE of 93% stations is less than 0.110, the MAE of 91% is less
936 than 0.060, and the R of 88% is greater than 0.70.

937 **2. Model validation.** For the daily scale, the R, RMSE and MAE between VIS_AOD and Aqua
938 AOD are 0.799, 0.079 and 0.044, respectively. The percentage of sample point falling within the EE
939 envelopes is 84.12%. The R between VIS_AOD and Terra AOD is 0.542, with a RMSE of 0.125
940 and MAE of 0.078. The percentage falling within the EE envelopes is 64.76%. The R between
941 VIS_AOD and AERONET AOD is 0.546, with a RMSE of 0.186 and MAE of 0.099. The percentage
942 falling within the EE envelopes is 57.87%. For the monthly and annual scales, RMSE and MAE
943 show a significant decrease between VIS_AOD and Aqua, Terra, and AERONET AOD, and R and
944 percentages falling within EE show a significant increase. Compared to AERONET AOD and
945 MERRA-2 AOD prior to 2000, the model has consistent predictive ability.

946 **3. Error analysis.** As the AOD value increases, the average bias increases. When the pollution level
947 is low ($AOD < 0.1$), the average bias is 0.015, with 83% of data within the EE envelopes. As
948 pollution level increases, the negative average bias becomes significant and the underestimation
949 increases. The elevation of AERONET's site also causes a bias. In low elevation (≤ 0.5 km), there
950 is a negative bias, with a percentage of 60%-64% falling within the EE envelopes. In high elevation
951 (0.5-1.2 km), there is a positive bias, with a percentage of 50%-65% falling within the EE envelopes.
952 When the elevation difference is negative (the elevation of the meteorological station is lower than
953 that of the AERONET site), there is a significant positive bias. When the difference is positive, the
954 mean bias approaches 0 or is positive. The influence of distance between the meteorological station
955 and AERONET site on bias is not significant.

956 **4. Global land AOD.** The mean AOD from 1980 to 2021 is 0.177 over land, 0.178 in the NH and
957 0.174 in the SH, with a trend of $-0.0029/10a$, $0.0030/10a$ and $-0.0021/10a$, respectively. The seasonal
958 AOD rankings are JJA (0.204) > MAM (0.176) > SON (0.164) > DJF (0.161) over global land, and
959 JJA (0.210) > MAM (0.176) > SON (0.163) > DJF (0.160) in the NH, SON (0.188) > DJF (0.184) >
960 MAM (0.14) > JJA (0.152) in the SH. The largest decreasing trends are in SON of the NH ($-$
961 $0.0064/10a$) and in JJA of the SH ($-0.0064/10a$). The increasing trends are in MAM of the NH and
962 in DJF and SON of the SH.

963 **5. Regional AOD.** The high aerosol loading ($AOD > 0.2$) regions are West Africa, Southeast and
964 Northeast Asia, Eastern China, and India, with a trend of $-0.0062/10a$, $0.0007/10a$, $-0.0009/10a$,
965 $0.0133/10a$, and $0.0119/10a$, respectively. However, the trends are decreasing in Eastern China ($-$

966 0.0572/10a) and Northeast Asia (-0.0213/10a) after 2014 and the larger increasing trend is found
967 after 2005 in India (0.0446/10a). The moderate aerosol loading (AOD between 0.15 and 0.2) regions
968 are Eastern Europe, Western Europe, Eastern North America, Central South America, and South
969 Africa, with a trend of -0.0067/10a, -0.0026/10a, -0.0027/10a, -0.0062/10a, and -0.0016/10a,
970 respectively. The low aerosol loading (AOD < 0.15) regions are Western North America and
971 Australia, with a trend of -0.0017/10a and -0.0028/10a. However, the trends in Southern Africa,
972 Southeast Asia and Northeast Asia are not significant.

973 **Competing interests**

974 The contact author has declared that none of the authors has any competing interests.

975 **Acknowledgments**

976 This work is supported by the National Key Research & Development Program of China
977 (2022YFF0801302) and the National Natural Science Foundation of China (41930970). The hourly
978 visibility data are downloaded from <https://mesonet.agron.iastate.edu/ASOS>. The Aerosol Robotic
979 Network (AERONET) 15-minute AOD data are downloaded from <https://aeronet.gsfc.nasa.gov>.
980 The MODIS AOD data are downloaded from <https://ladsweb.modaps.eosdis.nasa.gov>.

981 **References**

- 982 Ackerman, A. S., Hobbs, P. V., and Toon, O. B.: A model for particle microphysics, turbulent mixing,
983 and radiative transfer in the stratocumulus-topped marine boundary layer and comparisons with
984 measurements, *J. Atmos. Sci.*, 52, 1204-1236, [https://doi.org/10.1175/1520-
985 0469\(1995\)052<1204:AMFPMT>2.0.CO;2](https://doi.org/10.1175/1520-0469(1995)052<1204:AMFPMT>2.0.CO;2), 1995.
- 986 Albrecht, B. A.: Aerosols, cloud microphysics, and fractional cloudiness, *Science*, 245, 1227-1230,
987 <https://doi.org/10.1126/science.245.4923.1227>, 1989.
- 988 Anderson, T. L., Charlson, R. J., Bellouin, N., Boucher, O., Chin, M., Christopher, S. A., Haywood, J.,
989 Kaufman, Y. J., Kinne, S., Ogren, J. A., Remer, L. A., Takemura, T., Tanre, D., Torres, O., Trepte, C. R.,
990 Wielicki, B. A., Winker, D. M., and Yu, H. B.: An "A-Train" strategy for quantifying direct climate
991 forcing by anthropogenic aerosols, *B. Am. Meteorol. Soc.*, 86, 1795+, [https://doi.org/10.1175/Bams-86-
992 12-1795](https://doi.org/10.1175/Bams-86-12-1795), 2005.
- 993 Andersson, S. M., Martinsson, B. G., Vernier, J.-P., Friberg, J., Brenninkmeijer, C. A., Hermann, M., Van
994 Velthoven, P. F., and Zahn, A.: Significant radiative impact of volcanic aerosol in the lowermost
995 stratosphere, *Nat. Commun.*, 6, 7692, <https://doi.org/10.1038/ncomms8692>, 2015.
- 996 Andrews, E., Sheridan, P. J., Ogren, J. A., Hageman, D., Jefferson, A., Wendell, J., Alástuey, A., Alados-
997 Arboledas, L., Bergin, M., and Ealo, M.: Overview of the NOAA/ESRL federated aerosol network, *B.*
998 *Am. Meteorol. Soc.*, 100, 123-135, <https://doi.org/10.1175/BAMS-D-17-0175.1>, 2019.
- 999 Bergstrom, R. W., Pilewskie, P., Russell, P. B., Redemann, J., Bond, T. C., Quinn, P. K., and Sierau, B.:
1000 Spectral absorption properties of atmospheric aerosols, *Atmos. Chem. Phys.*, 7, 5937-5943,
1001 <https://doi.org/10.5194/acp-7-5937-2007>, 2007.
- 1002 Berk, R. A.: Classification and Regression Trees (CART), in: *Statistical Learning from a Regression*
1003 *Perspective*, Springer New York, New York, NY, 1-65, https://doi.org/10.1007/978-0-387-77501-2_3,

1004 2008.

1005 Bescond, A., Yon, J., Girasole, T., Jouen, C., Rozé, C., and Coppalle, A.: Numerical investigation of the
1006 possibility to determine the primary particle size of fractal aggregates by measuring light depolarization,
1007 *J. Quant. Spectrosc. Ra.*, 126, 130-139, <https://doi.org/10.1016/j.jqsrt.2012.10.011>, 2013.

1008 Boers, R., van Weele, M., van Meijgaard, E., Savenije, M., Siebesma, A. P., Bosveld, F., and Stammes,
1009 P.: Observations and projections of visibility and aerosol optical thickness (1956-2100) in the
1010 Netherlands: impacts of time-varying aerosol composition and hygroscopicity, *Environ. Res. Lett.*, 10,
1011 <https://doi.org/10.1088/1748-9326/10/1/015003>, 2015.

1012 Bokoye, A. I., Royer, A., O'Neil, N., Cliche, P., Fedosejevs, G., Teillet, P., and McArthur, L.:
1013 Characterization of atmospheric aerosols across Canada from a ground-based sunphotometer network:
1014 AEROCAN, *Atmos. Ocean*, 39, 429-456, <https://doi.org/10.1080/07055900.2001.9649687>, 2001.

1015 Bösenberg, J. and Matthias, V.: EARLINET: A European Aerosol Research Lidar Network to Establish
1016 an Aerosol Climatology, Max Planck Institut Fur Meteorologie, 2003.

1017 Bright, J. M. and Gueymard, C. A.: Climate-specific and global validation of MODIS Aqua and Terra
1018 aerosol optical depth at 452 AERONET stations, *Sol. Energy*, 183, 594-605,
1019 <https://doi.org/10.1016/j.solener.2019.03.043>, 2019.

1020 Browne, M. W.: Cross-validation methods, *J. Math. Psychol.*, 44, 108-132,
1021 <https://doi.org/10.1006/jmps.1999.1279>, 2000.

1022 Calvo, A. I., Alves, C., Castro, A., Pont, V., Vicente, A. M., and Fraile, R.: Research on aerosol sources
1023 and chemical composition: Past, current and emerging issues, *Atmos. Res.*, 120, 1-28,
1024 <https://doi.org/10.1016/j.atmosres.2012.09.021>, 2013.

1025 Chafe, Z. A., Brauer, M., Klimont, Z., Van Dingenen, R., Mehta, S., Rao, S., Riahi, K., Dentener, F., and
1026 Smith, K. R.: Household Cooking with Solid Fuels Contributes to Ambient PM_{2.5} Air Pollution and the
1027 Burden of Disease, *Environ. Health Persp.*, 122, 1314-1320, <https://doi.org/10.1289/ehp.1206340>, 2014.

1028 Chazette, P., David, C., Lefrère, J., Godin, S., Pelon, J., and Mégie, G.: Comparative lidar study of the
1029 optical, geometrical, and dynamical properties of stratospheric post-volcanic aerosols, following the
1030 eruptions of El Chichon and Mount Pinatubo, *J. Geophys. Res-Atmos.*, 100, 23195-23207,
1031 <https://doi.org/10.1029/95JD02268>, 1995.

1032 Che, H., Zhang, X., Chen, H., Damiri, B., Goloub, P., Li, Z., Zhang, X., Wei, Y., Zhou, H., Dong, F., Li,
1033 D., and Zhou, T.: Instrument calibration and aerosol optical depth validation of the China Aerosol Remote
1034 Sensing Network, *J. Geophys. Res-Atmos.*, 114, <https://doi.org/10.1029/2008jd011030>, 2009.

1035 Che, H., Xia, X., Zhu, J., Li, Z., Dubovik, O., Holben, B., Goloub, P., Chen, H., Estelles, V., Cuevas-
1036 Agullo, E., Blarel, L., Wang, H., Zhao, H., Zhang, X., Wang, Y., Sun, J., Tao, R., Zhang, X., and Shi, G.:
1037 Column aerosol optical properties and aerosol radiative forcing during a serious haze-fog month over
1038 North China Plain in 2013 based on ground-based sunphotometer measurements, *Atmos. Chem. Phys.*,
1039 14, 2125-2138, <https://doi.org/10.5194/acp-14-2125-2014>, 2014.

1040 Chen, A., Zhao, C., and Fan, T.: Spatio-temporal distribution of aerosol direct radiative forcing over mid-
1041 latitude regions in north hemisphere estimated from satellite observations, *Atmos. Res.*, 266, 105938,
1042 <https://doi.org/10.1016/j.atmosres.2021.105938>, 2022.

1043 Chen, D., Ou, T., Gong, L., Xu, C.-Y., Li, W., Ho, C.-H., and Qian, W.: Spatial Interpolation of Daily
1044 Precipitation in China: 1951-2005, *Adv. Atmos. Sci.*, 27, 1221-1232, <https://doi.org/10.1007/s00376-010-9151-y>, 2010.

1045
1046 Cherian, R. and Quaas, J.: Trends in AOD, clouds, and cloud radiative effects in satellite data and CMIP5
1047 and CMIP6 model simulations over aerosol source regions, *Geophys. Res. Lett.*, 47, e2020GL087132,

1048 <https://doi.org/10.1029/2020GL087132>, 2020.

1049 Chin, M., Diehl, T., Tan, Q., Prospero, J., Kahn, R., Remer, L., Yu, H., Sayer, A., Bian, H., and
1050 Geogdzhayev, I.: Multi-decadal aerosol variations from 1980 to 2009: a perspective from observations
1051 and a global model, *Atmos. Chem. Phys.*, 14, 3657-3690, <https://doi.org/10.5194/acp-14-3657-2014>,
1052 2014.

1053 Chu, D., Kaufman, Y., Ichoku, C., Remer, L., Tanré, D., and Holben, B.: Validation of MODIS aerosol
1054 optical depth retrieval over land, *Geophys. Res. Lett.*, 29, MOD2-1-MOD2-4,
1055 <https://doi.org/10.1029/2001GL013205>, 2002.

1056 Chuang, P.-J. and Huang, P.-Y.: B-VAE: a new dataset balancing approach using batched Variational
1057 AutoEncoders to enhance network intrusion detection, *J. Supercomput.*, <https://doi.org/10.1007/s11227-023-05171-w>, 2023.

1059 Deuzé, J., Goloub, P., Herman, M., Marchand, A., Perry, G., Susana, S., and Tanré, D.: Estimate of the
1060 aerosol properties over the ocean with POLDER, *J. Geophys. Res-Atmos.*, 105, 15329-15346,
1061 <https://doi.org/10.1029/2000JD900148>, 2000.

1062 Dhanya, R., Paul, I. R., Akula, S. S., Sivakumar, M., and Nair, J. J.: F-test feature selection in Stacking
1063 ensemble model for breast cancer prediction, *Procedia. Comput. Sci.*, 171, 1561-1570,
1064 <https://doi.org/10.1016/j.procs.2020.04.167>, 2020.

1065 Diner, D. J., Beckert, J. C., Reilly, T. H., Bruegge, C. J., Conel, J. E., Kahn, R. A., Martonchik, J. V.,
1066 Ackerman, T. P., Davies, R., and Gerstl, S. A. W.: Multi-angle Imaging SpectroRadiometer (MISR)
1067 instrument description and experiment overview, *Ieee T. Geosci. Remote.*, 98, 1072-1087,
1068 <https://doi.org/10.1109/36.700992>, 1998.

1069 Dong, Y., Li, J., Yan, X., Li, C., Jiang, Z., Xiong, C., Chang, L., Zhang, L., Ying, T., and Zhang, Z.:
1070 Retrieval of aerosol single scattering albedo using joint satellite and surface visibility measurements,
1071 *Remote Sens. Environ.*, 294, 113654, <https://doi.org/10.1016/j.rse.2023.113654>, 2023.

1072 Dubovik, Oleg, Holben, Brent, Eck, Thomas, F., Smirnov, Alexander, and Kaufman: Variability of
1073 Absorption and Optical Properties of Key Aerosol Types Observed in Worldwide Locations, *J. Atmos.*
1074 *Sci.*, 59, 590-590, [https://doi.org/10.1175/1520-0469\(2002\)059<0590:VOAAOP>2.0.CO;2](https://doi.org/10.1175/1520-0469(2002)059<0590:VOAAOP>2.0.CO;2), 2002a.

1075 Dubovik, O., Smirnov, A., Holben, B. N., King, M. D., Kaufman, Y. J., Eck, T. F., and Slutsker, I.:
1076 Accuracy assessments of aerosol optical properties retrieved from Aerosol Robotic Network (AERONET)
1077 Sun and sky radiance measurements, *J. Geophys. Res-Atmos.*, 105, 9791-9806,
1078 <https://doi.org/10.1029/2000jd900040>, 2000.

1079 Dubovik, O., Holben, B., Eck, T. F., Smirnov, A., Kaufman, Y. J., King, M. D., Tanré, D., and Slutsker,
1080 I.: Variability of absorption and optical properties of key aerosol types observed in worldwide locations,
1081 *J. Atmos. Sci.*, 59, 590-608, [https://doi.org/10.1175/1520-0469\(2002\)059<0590:VOAAOP>2.0.CO;2](https://doi.org/10.1175/1520-0469(2002)059<0590:VOAAOP>2.0.CO;2),
1082 2002b.

1083 Eck, T. F., Holben, B. N., Reid, J. S., Sinyuk, A., Giles, D. M., Arola, A., Slutsker, I., Schafer, J. S.,
1084 Sorokin, M. G., and Smirnov, A.: The extreme forest fires in California/Oregon in 2020: Aerosol optical
1085 and physical properties and comparisons of aged versus fresh smoke, *Atmos. Environ.*, 305, 119798,
1086 <https://doi.org/10.1016/j.atmosenv.2023.119798>, 2023.

1087 Elterman, L.: Relationships between vertical attenuation and surface meteorological range, *Appl. Optics*,
1088 9, 1804-1810, <https://doi.org/10.1364/AO.9.001804>, 1970.

1089 Fan, H., Zhao, C., Yang, Y., and Yang, X.: Spatio-Temporal Variations of the
1090 PM_{2.5}/PM₁₀ Ratios and Its Application to Air Pollution Type Classification
1091 in China, *Front. Environ. Sci.*, 9, <https://doi.org/10.3389/fenvs.2021.692440>, 2021.

1092 Fernández, A., Garcia, S., Herrera, F., and Chawla, N. V.: SMOTE for learning from imbalanced data:
1093 progress and challenges, marking the 15-year anniversary, *J. Artif. Intell. Res.*, 61, 863-905,
1094 <https://doi.org/10.1613/jair.1.11192>, 2018.

1095 Forster, P., Ramaswamy, V., Artaxo, P., Berntsen, T., Betts, R., Fahey, D. W., Haywood, J., Lean, J., Lowe,
1096 D. C., and Myhre, G.: Changes in atmospheric constituents and in radiative forcing, *Climate Change*
1097 *2007: The Physical Science Basis. Contribution of Working Group I to the 4th Assessment Report of the*
1098 *Intergovernmental Panel on Climate Change*, 2007.

1099 Gelaro, R., McCarty, W., Suárez, M. J., Todling, R., Molod, A., Takacs, L., Randles, C. A., Darmenov,
1100 A., Bosilovich, M. G., Reichle, R., Wargan, K., Coy, L., Cullather, R., Draper, C., Akella, S., Buchard,
1101 V., Conaty, A., da Silva, A. M., Gu, W., Kim, G.-K., Koster, R., Lucchesi, R., Merkova, D., Nielsen, J.
1102 E., Partyka, G., Pawson, S., Putman, W., Rienecker, M., Schubert, S. D., Sienkiewicz, M., and Zhao, B.:
1103 The Modern-Era Retrospective Analysis for Research and Applications, Version 2 (MERRA-2), *J.*
1104 *Climate*, 30, 5419-5454, <https://doi.org/10.1175/JCLI-D-16-0758.1>, 2017.

1105 Giglio, L., Randerson, J. T., and Van Der Werf, G. R.: Analysis of daily, monthly, and annual burned area
1106 using the fourth-generation global fire emissions database (GFED4), *J. Geophys. Res-Biogeo.*, 118, 317-
1107 328, <https://doi.org/10.1002/jgrg.20042>, 2013.

1108 Giles, D. M., Sinyuk, A., Sorokin, M. G., Schafer, J. S., Smirnov, A., Slutsker, I., Eck, T. F., Holben, B.
1109 N., Lewis, J. R., Campbell, J. R., Welton, E. J., Korkin, S. V., and Lyapustin, A. I.: Advancements in the
1110 Aerosol Robotic Network (AERONET) Version 3 database – automated near-real-time quality control
1111 algorithm with improved cloud screening for Sun photometer aerosol optical depth (AOD) measurements,
1112 *Atmos. Meas. Tech.*, 12, 169-209, <https://doi.org/10.5194/amt-12-169-2019>, 2019.

1113 Goovaerts, P.: Geostatistical approaches for incorporating elevation into the spatial interpolation of
1114 rainfall, *Journal of Hydrology*, 228, 113-129, [https://doi.org/10.1016/s0022-1694\(00\)00144-x](https://doi.org/10.1016/s0022-1694(00)00144-x), 2000.

1115 Gras, J., Jensen, J., Okada, K., Ikegami, M., Zaizen, Y., and Makino, Y.: Some optical properties of smoke
1116 aerosol in Indonesia and tropical Australia, *Geophys. Res. Lett.*, 26, 1393-1396,
1117 <https://doi.org/10.1029/1999GL900275>, 1999.

1118 Guerrero-Rascado, J. L., Landulfo, E., Antuña, J. C., Barbosa, H. d. M. J., Barja, B., Bastidas, Á. E.,
1119 Bedoya, A. E., da Costa, R. F., Estevan, R., and Forno, R.: Latin American Lidar Network (LALINET)
1120 for aerosol research: Diagnosis on network instrumentation, *J. Atmos. Sol-Terr. Phys.*, 138, 112-120,
1121 <https://doi.org/10.1016/j.jastp.2016.01.001>, 2016.

1122 Guo, J., Zhang, J., Yang, K., Liao, H., Zhang, S., Huang, K., Lv, Y., Shao, J., Yu, T., and Tong, B.:
1123 Investigation of near-global daytime boundary layer height using high-resolution radiosondes: first
1124 results and comparison with ERA5, MERRA-2, JRA-55, and NCEP-2 reanalyses, *Atmos. Chem. Phys.*,
1125 21, 17079-17097, <https://doi.org/10.5194/acp-21-17079-2021>, 2021.

1126 Hao, H., Wang, K., and Wu, G.: Visibility-derived aerosol optical depth over global land (1980-2021),
1127 *National Tibetan Plateau Data Center [dataset]*, <https://doi.org/10.11888/Atmos.tpdc.300822>, 2023.

1128 He, H., Bai, Y., Garcia, E. A., and Li, S.: ADASYN: Adaptive synthetic sampling approach for
1129 imbalanced learning, *IEEE World Congress on Computational Intelligence*, 1322-1328,
1130 <https://doi.org/10.1109/IJCNN.2008.4633969>, 2008.

1131 Hersbach, H., Bell, B., Berrisford, P., Hirahara, S., Horányi, A., Muñoz-Sabater, J., Nicolas, J., Peubey,
1132 C., Radu, R., and Schepers, D.: The ERA5 global reanalysis, *Q. J. Roy. Meteor. Soc.*, 146, 1999-2049,
1133 <https://doi.org/10.1002/qj.3803>, 2020.

1134 Hersey, S. P., Garland, R. M., Crosbie, E., Shingler, T., Sorooshian, A., Piketh, S., and Burger, R.: An
1135 overview of regional and local characteristics of aerosols in South Africa using satellite, ground, and

1136 modeling data, *Atmos. Chem. Phys.*, 15, 4259-4278, <https://doi.org/10.5194/acp-15-4259-2015>, 2015.

1137 Hirono, M. and Shibata, T.: Enormous increase of stratospheric aerosols over Fukuoka due to volcanic
1138 eruption of El Chichon in 1982, *Geophys. Res. Lett.*, 10, 152-154,
1139 <https://doi.org/10.1029/GL010i002p00152>, 1983.

1140 Hofmann, D., Barnes, J., O'Neill, M., Trudeau, M., and Neely, R.: Increase in background stratospheric
1141 aerosol observed with lidar at Mauna Loa Observatory and Boulder, Colorado, *Geophys. Res. Lett.*, 36,
1142 <https://doi.org/10.1029/2009GL039008>, 2009.

1143 Holben, B. N., Eck, T. F., Slutsker, I., Tanre, D., Buis, J. P., Setzer, A., Vermote, E., Reagan, J. A.,
1144 Kaufman, Y. J., Nakajima, T., Lavenu, F., Jankowiak, I., and Smirnov, A.: AERONET - A federated
1145 instrument network and data archive for aerosol characterization, *Remote Sens. Environ.*, 66, 1-16,
1146 [https://doi.org/10.1016/s0034-4257\(98\)00031-5](https://doi.org/10.1016/s0034-4257(98)00031-5), 1998.

1147 Hsu, N., Gautam, R., Sayer, A., Bettenhausen, C., Li, C., Jeong, M., Tsay, S.-C., and Holben, B.: Global
1148 and regional trends of aerosol optical depth over land and ocean using SeaWiFS measurements from
1149 1997 to 2010, *Atmos. Chem. Phys.*, 12, 8037-8053, <https://doi.org/10.5194/acp-12-8037-2012>, 2012.

1150 Hsu, N., Jeong, M. J., Bettenhausen, C., Sayer, A., Hansell, R., Seftor, C., Huang, J., and Tsay, S. C.:
1151 Enhanced Deep Blue aerosol retrieval algorithm: The second generation, *J. Geophys. Res-Atmos.*, 118,
1152 9296-9315, <https://doi.org/10.1002/jgrd.50712>, 2013.

1153 Hsu, N., Lee, J., Sayer, A., Carletta, N., Chen, S. H., Tucker, C., Holben, B., and Tsay, S. C.: Retrieving
1154 near-global aerosol loading over land and ocean from AVHRR, *J. Geophys. Res-Atmos.*, 122, 9968-
1155 9989, <https://doi.org/10.1002/2017JD026932>, 2017.

1156 Hsu, N. C., Tsay, S.-C., King, M. D., and Herman, J. R.: Deep blue retrievals of Asian aerosol properties
1157 during ACE-Asia, *Ieee T. Geosci. Remote.*, 44, 3180-3195, <https://doi.org/10.1109/tgrs.2006.879540>,
1158 2006.

1159 Hu, B., Zhang, X., Sun, R., and Zhu, X.: Retrieval of Horizontal Visibility Using MODIS Data: A Deep
1160 Learning Approach, *Atmosphere-Basel*, 10, <https://doi.org/10.3390/atmos10120740>, 2019.

1161 Hu, K., Kumar, K. R., Kang, N., Boiyo, R., and Wu, J.: Spatiotemporal characteristics of aerosols and
1162 their trends over mainland China with the recent Collection 6 MODIS and OMI satellite datasets, *Environ.*
1163 *Sci. Pollut. R.*, 25, 6909-6927, <https://doi.org/10.1007/s11356-017-0715-6>, 2018.

1164 Husar, R. B., Husar, J. D., and Martin, L.: Distribution of continental surface aerosol extinction based on
1165 visual range data, *Atmos. Environ.*, 34, 5067-5078, [https://doi.org/10.1016/s1352-2310\(00\)00324-1](https://doi.org/10.1016/s1352-2310(00)00324-1),
1166 2000.

1167 IPCC: *Climate Change 2021: The Physical Science Basis*, Cambridge University Press, New York, 2021.

1168 Ivanova, G., Ivanov, V., Kukavskaya, E., and Soja, A.: The frequency of forest fires in Scots pine stands
1169 of Tuva, Russia, *Environ. Res. Lett.*, 5, 015002, <https://doi.org/10.1088/1748-9326/5/1/015002>, 2010.

1170 Kang, Y., Kim, M., Kang, E., Cho, D., and Im, J.: Improved retrievals of aerosol optical depth and fine
1171 mode fraction from GOCI geostationary satellite data using machine learning over East Asia, *Isprs J.*
1172 *Photogramm.*, 183, 253-268, <https://doi.org/10.1016/j.isprsjprs.2021.11.016>, 2022.

1173 Kang, Y., Choi, H., Im, J., Park, S., Shin, M., Song, C.-K., and Kim, S.: Estimation of surface-level NO₂
1174 and O₃ concentrations using TROPOMI data and machine learning over East Asia, *Environ. Pollut.*, 288,
1175 117711, <https://doi.org/10.1016/j.envpol.2021.117711>, 2021.

1176 Karbowska, B. and Zembrzuski, W.: Fractionation and mobility of thallium in volcanic ashes after
1177 eruption of Eyjafjallajökull (2010) in Iceland, *B. Environ. Contam. Tox.*, 97, 37-43,
1178 <https://doi.org/10.1007/s00128-016-1831-6>, 2016.

1179 Kaufman, Y. J. and Boucher, O.: A satellite view of aerosols in the climate system, *Nature*, 419, 215-215,

1180 <https://doi.org/10.1038/nature01091>, 2002.

1181 Kim, D. H., Sohn, B. J., Nakajima, T., Takamura, T., Takemura, T., Choi, B. C., and Yoon, S. C.: Aerosol
1182 optical properties over east Asia determined from ground-based sky radiation measurements, *J. Geophys.*
1183 *Res-Atmos.*, 109, <https://doi.org/10.1029/2003jd003387>, 2004.

1184 Klett, J. D.: Lidar inversion with variable backscatter/extinction ratios, *Appl. Optics*, 24, 1638-1643,
1185 <https://doi.org/10.1364/AO.24.001638>, 1985.

1186 Koelemeijer, R., Homan, C., and Matthijsen, J.: Comparison of spatial and temporal variations of aerosol
1187 optical thickness and particulate matter over Europe, *Atmos. Environ.*, 40, 5304-5315,
1188 <https://doi.org/10.1016/j.atmosenv.2006.04.044>, 2006.

1189 Koschmieder, H.: Theorie der horizontalen Sichtweite, *Beitrage zur Physik der freien Atmosphere*, 12,
1190 33-55, 1924.

1191 Krylov, A., McCarty, J. L., Potapov, P., Loboda, T., Tyukavina, A., Turubanova, S., and Hansen, M. C.:
1192 Remote sensing estimates of stand-replacement fires in Russia, 2002–2011, *Environ. Res. Lett.*, 9,
1193 105007, <https://doi.org/10.1088/1748-9326/9/10/105007>, 2014.

1194 Kulmala, M., Vehkamäki, H., Petäjä, T., Dal Maso, M., Lauri, A., Kerminen, V. M., Birmili, W., and
1195 McMurry, P. H.: Formation and growth rates of ultrafine atmospheric particles: A review of observations,
1196 *J. Aerosol Sci.*, 35, 143-176, <https://doi.org/10.1016/j.jaerosci.2003.10.003>, 2004.

1197 Kumm, M., De Moel, H., Salvucci, G., Viviroli, D., Ward, P. J., and Varis, O.: Over the hills and further
1198 away from coast: global geospatial patterns of human and environment over the 20th–21st centuries,
1199 *Environ. Res. Lett.*, 11, 034010, <https://doi.org/10.1088/1748-9326/11/3/034010>, 2016.

1200 Lapen, D. R. and Hayhoe, H. N.: Spatial analysis of seasonal and annual temperature and precipitation
1201 normals in southern Ontario, Canada, *J. Great Lakes Res.*, 29, 529-544, [https://doi.org/10.1016/s0380-1330\(03\)70457-2](https://doi.org/10.1016/s0380-1330(03)70457-2), 2003.

1203 Lee, L. A., Reddington, C. L., and Carslaw, K. S.: On the relationship between aerosol model uncertainty
1204 and radiative forcing uncertainty, *P. Natl. A. Sci.*, 113, 5820-5827,
1205 <https://doi.org/10.1073/pnas.1507050113>, 2016.

1206 Levy, R., Remer, L., Kleidman, R., Mattoo, S., Ichoku, C., Kahn, R., and Eck, T.: Global evaluation of
1207 the Collection 5 MODIS dark-target aerosol products over land, *Atmos. Chem. Phys.*, 10, 10399-10420,
1208 <https://doi.org/10.5194/acp-10-10399-2010>, 2010.

1209 Levy, R. C., Remer, L. A., Mattoo, S., Vermote, E. F., and Kaufman, Y. J.: Second-generation operational
1210 algorithm: Retrieval of aerosol properties over land from inversion of Moderate Resolution Imaging
1211 Spectroradiometer spectral reflectance, *J. Geophys. Res-Atmos.*, 112,
1212 <https://doi.org/10.1029/2006JD007811>, 2007.

1213 Levy, R. C., Mattoo, S., Munchak, L. A., Remer, L. A., Sayer, A. M., Patadia, F., and Hsu, N. C.: The
1214 Collection 6 MODIS aerosol products over land and ocean, *Atmos. Meas. Tech.*, 6, 2989-3034,
1215 <https://doi.org/10.5194/amt-6-2989-2013>, 2013.

1216 Levy, R. C., Mattoo, S., Sawyer, V., Shi, Y., Colarco, P. R., Lyapustin, A. I., Wang, Y., and Remer, L. A.:
1217 Exploring systematic offsets between aerosol products from the two MODIS sensors, *Atmos. Meas. Tech.*,
1218 11, 4073-4092, <https://doi.org/10.5194/amt-11-4073-2018>, 2018.

1219 Li, J., Garshick, E., Hart, J. E., Li, L., Shi, L., Al-Hemoud, A., Huang, S., and Koutrakis, P.: Estimation
1220 of ambient PM_{2.5} in Iraq and Kuwait from 2001 to 2018 using machine learning and remote sensing,
1221 *Environ. Int.*, 151, <https://doi.org/10.1016/j.envint.2021.106445>, 2021.

1222 Li, J., Carlson, B. E., Yung, Y. L., Lv, D., Hansen, J., Penner, J. E., Liao, H., Ramaswamy, V., Kahn, R.
1223 A., Zhang, P., Dubovik, O., Ding, A., Lacis, A. A., Zhang, L., and Dong, Y.: Scattering and absorbing

1224 aerosols in the climate system, *Nat. Rev. Earth. Environ.*, 3, 363-379, [https://doi.org/10.1038/s43017-](https://doi.org/10.1038/s43017-022-00296-7)
1225 [022-00296-7](https://doi.org/10.1038/s43017-022-00296-7), 2022.

1226 Li, S., Chen, L., Huang, G., Lin, J., Yan, Y., Ni, R., Huo, Y., Wang, J., Liu, M., and Weng, H.: Retrieval
1227 of surface PM_{2.5} mass concentrations over North China using visibility measurements and GEOS-Chem
1228 simulations, *Atmos. Environ.*, 222, 117121, <https://doi.org/10.1016/j.atmosenv.2019.117121>, 2020.

1229 Li, Z., Lau, W. M., Ramanathan, V., Wu, G., Ding, Y., Manoj, M., Liu, J., Qian, Y., Li, J., and Zhou, T.:
1230 Aerosol and monsoon climate interactions over Asia, *Rev. Geophys.*, 54, 866-929,
1231 <https://doi.org/10.1002/2015RG000500>, 2016.

1232 Liao, H., Chang, W., and Yang, Y.: Climatic Effects of Air Pollutants over China: A Review, *Adv. Atmos.*
1233 *Sci.*, 32, 115-139, <https://doi.org/10.1007/s00376-014-0013-x>, 2015.

1234 Lin, J. T., van Donkelaar, A., Xin, J. Y., Che, H. Z., and Wang, Y. S.: Clear-sky aerosol optical depth over
1235 East China estimated from visibility measurements and chemical transport modeling, *Atmos. Environ.*,
1236 95, 258-267, <https://doi.org/10.1016/j.atmosenv.2014.06.044>, 2014.

1237 Liu, B., Ma, X., Ma, Y., Li, H., Jin, S., Fan, R., and Gong, W.: The relationship between atmospheric
1238 boundary layer and temperature inversion layer and their aerosol capture capabilities, *Atmos. Res.*, 271,
1239 <https://doi.org/10.1016/j.atmosres.2022.106121>, 2022.

1240 Mahowald, N. M., Ballantine, J. A., Feddema, J., and Ramankutty, N.: Global trends in visibility:
1241 implications for dust sources, *Atmos. Chem. Phys.*, 7, 3309-3339, [https://doi.org/10.5194/acp-7-3309-](https://doi.org/10.5194/acp-7-3309-2007)
1242 [2007](https://doi.org/10.5194/acp-7-3309-2007), 2007.

1243 McNeill, V. F.: Atmospheric Aerosols: Clouds, Chemistry, and Climate, in: *Annu. Rev. Chem. Biomol.*,
1244 edited by: Prausnitz, J. M., *Annual Review of Chemical and Biomolecular Engineering*, 427-444,
1245 <https://doi.org/10.1146/annurev-chembioeng-060816-101538>, 2017.

1246 Mehta, M., Singh, R., Singh, A., and Singh, N.: Recent global aerosol optical depth variations and
1247 trends—A comparative study using MODIS and MISR level 3 datasets, *Remote Sens. Environ.*, 181,
1248 137-150, <https://doi.org/10.1016/j.rse.2016.04.004>, 2016.

1249 Mitra, R., Bajpai, A., and Biswas, K.: ADASYN-assisted machine learning for phase prediction of high
1250 entropy carbides, *Comp. Mater. Sci.*, 223, <https://doi.org/10.1016/j.commatsci.2023.112142>, 2023.

1251 Mortier, A., Gliß, J., Schulz, M., Aas, W., Andrews, E., Bian, H., Chin, M., Ginoux, P., Hand, J., and
1252 Holben, B.: Evaluation of climate model aerosol trends with ground-based observations over the last 2
1253 decades—an AeroCom and CMIP6 analysis, *Atmos. Chem. Phys.*, 20, 13355-13378,
1254 <https://doi.org/10.5194/acp-20-13355-2020>, 2020.

1255 Mukkavilli, S., Prasad, A., Taylor, R., Huang, J., Mitchell, R., Troccoli, A., and Kay, M.: Assessment of
1256 atmospheric aerosols from two reanalysis products over Australia, *Atmos. Res.*, 215, 149-164,
1257 <https://doi.org/10.1016/j.atmosres.2018.08.026>, 2019.

1258 Nagaraja Rao, C., Stowe, L., and McClain, E.: Remote sensing of aerosols over the oceans using AVHRR
1259 data Theory, practice and applications, *Int. J. Remote Sens.*, 10, 743-749,
1260 <https://doi.org/10.1080/01431168908903915>, 1989.

1261 Nakajima, T., Campanelli, M., Che, H., Estellés, V., Irie, H., Kim, S.-W., Kim, J., Liu, D., Nishizawa, T.,
1262 and Pandithurai, G.: An overview of and issues with sky radiometer technology and SKYNET, *Atmos.*
1263 *Meas. Tech.*, 13, 4195-4218, <https://doi.org/10.5194/amt-13-4195-2020>, 2020.

1264 NOAA, DOD, FAA, and USN: Automated Surface Observing System (ASOS) User's Guide, 1998.

1265 O'Reilly, J. E., Maritorena, S., Mitchell, B. G., Siegel, D. A., Carder, K. L., Garver, S. A., Kahru, M., and
1266 McClain, C.: Ocean color chlorophyll algorithms for SeaWiFS, *J. Geophys. Res.*, 103, 24937-24953,
1267 <https://doi.org/10.1029/98jc02160>, 1998.

1268 Pebesma, E. J.: Multivariable geostatistics in S: the gstat package, *Comput. Geosci.*, 30, 683-691,
1269 <https://doi.org/10.1016/j.cageo.2004.03.012>, 2004.

1270 Qiu, J. and Lin, Y.: A parameterization model of aerosol optical depths in China, *Acta. Meteorol. Sin.*,
1271 59, 368-372, <https://doi.org/10.11676/qxxb2001.039>, 2001.

1272 Ramanathan, V., Crutzen, P. J., Kiehl, J., and Rosenfeld, D.: Aerosols, climate, and the hydrological cycle,
1273 *Science*, 294, 2119-2124, <https://doi.org/10.1126/science.1064034>, 2001.

1274 Remer, L. A., Kleidman, R. G., Levy, R. C., Kaufman, Y. J., Tanre, D., Mattoo, S., Martins, J. V., Ichoku,
1275 C., Koren, I., Yu, H., and Holben, B. N.: Global aerosol climatology from the MODIS satellite sensors,
1276 *J. Geophys. Res-Atmos.*, 113, <https://doi.org/10.1029/2007jd009661>, 2008.

1277 Remer, L. A., Kaufman, Y. J., Tanre, D., Mattoo, S., Chu, D. A., Martins, J. V., Li, R. R., Ichoku, C.,
1278 Levy, R. C., Kleidman, R. G., Eck, T. F., Vermote, E., and Holben, B. N.: The MODIS aerosol algorithm,
1279 products, and validation, *J. Atmos. Sci.*, 62, 947-973, <https://doi.org/10.1175/jas3385.1>, 2005.

1280 Salomonson, V. V., Barnes, W. L., Maymon, P. W., Montgomery, H. E., and Ostrow, H.: MODIS:
1281 advanced facility instrument for studies of the Earth as a system, *Ieee T. Geosci. Remote.*, 27, 145-153,
1282 <https://doi.org/10.1109/36.20292>, 1987.

1283 Sawamura, P., Vernier, J. P., Barnes, J. E., Berkoff, T. A., Welton, E. J., Alados-Arboledas, L., Navas-
1284 Guzmán, F., Pappalardo, G., Mona, L., and Madonna, F.: Stratospheric AOD after the 2011 eruption of
1285 Nabro volcano measured by lidars over the Northern Hemisphere, *Environ. Res. Lett.*, 7, 34013-
1286 34021(34019), <https://doi.org/10.1088/1748-9326/7/3/034013>, 2012.

1287 Schutgens, N., Tsyro, S., Gryspeerdt, E., Goto, D., Weigum, N., Schulz, M., and Stier, P.: On the spatio-
1288 temporal representativeness of observations, *Atmos. Chem. Phys.*, 17, 9761-9780,
1289 <https://doi.org/10.5194/acp-17-9761-2017>, 2017.

1290 Singh, A., Mahata, K. S., Rupakheti, M., Junkermann, W., Panday, A. K., and Lawrence, M. G.: An
1291 overview of airborne measurement in Nepal—Part 1: Vertical profile of aerosol size, number, spectral
1292 absorption, and meteorology, *Atmos. Chem. Phys.*, 19, 245-258, [https://doi.org/10.5194/acp-19-245-](https://doi.org/10.5194/acp-19-245-2019)
1293 [2019](https://doi.org/10.5194/acp-19-245-2019), 2019.

1294 Smirnov, A., Holben, B., Slutsker, I., Giles, D., McClain, C., Eck, T., Sakerin, S., Macke, A., Croot, P.,
1295 and Zibordi, G.: Maritime aerosol network as a component of aerosol robotic network, *J. Geophys. Res-*
1296 *Atmos.*, 114, <https://doi.org/10.1029/2008JD011257>, 2009.

1297 Streets, D. G., Yan, F., Chin, M., Diehl, T., Mahowald, N., Schultz, M., Wild, M., Wu, Y., and Yu, C.:
1298 Anthropogenic and natural contributions to regional trends in aerosol optical depth, 1980–2006, *J.*
1299 *Geophys. Res-Atmos.*, 114, <https://doi.org/10.1029/2008JD011624>, 2009.

1300 Sun, E., Xu, X., Che, H., Tang, Z., Gui, K., An, L., Lu, C., and Shi, G.: Variation in MERRA-2 aerosol
1301 optical depth and absorption aerosol optical depth over China from 1980 to 2017, *J. Atmos. Sol-Terr.*
1302 *Phy.*, 186, 8-19, <https://doi.org/10.1016/j.jastp.2019.01.019>, 2019.

1303 Sun, Y. and Zhao, C.: Influence of Saharan dust on the large-scale meteorological environment for
1304 development of tropical cyclone over North Atlantic Ocean Basin, *J. Geophys. Res-Atmos.*, 125,
1305 e2020JD033454, <https://doi.org/10.1029/2020JD033454>, 2020.

1306 Teixeira, A.: Classification and regression tree, *Rev. Mal. Respir.*, 21, 1174-1176,
1307 [https://doi.org/10.1016/S0761-8425\(04\)71596-X](https://doi.org/10.1016/S0761-8425(04)71596-X), 2004.

1308 Tian, X., Tang, C., Wu, X., Yang, J., Zhao, F., and Liu, D.: The global spatial-temporal distribution and
1309 EOF analysis of AOD based on MODIS data during 2003-2021, *Atmos. Environ.*, 302,
1310 <https://doi.org/10.1016/j.atmosenv.2023.119722>, 2023.

1311 Tupper, A., Oswalt, J. S., and Rosenfeld, D.: Satellite and radar analysis of the volcanic-cumulonimbi at

1312 Mount Pinatubo, Philippines, 1991, J. Geophys. Res-Atmos., 110,
1313 <https://doi.org/10.1029/2004JD005499>, 2005.

1314 van der Veer, G., Voerkelius, S., Lorentz, G., Heiss, G., and Hoogewerff, J. A.: Spatial interpolation of
1315 the deuterium and oxygen-18 composition of global precipitation using temperature as ancillary variable,
1316 Journal of Geochemical Exploration, 101, 175-184, <https://doi.org/10.1016/j.gexplo.2008.06.008>, 2009.

1317 Vernier, J. P., Thomason, L. W., Pommereau, J. P., Bourassa, A., Pelon, J., Garnier, A., Hauchecorne, A.,
1318 Blanot, L., Trepte, C., and Degenstein, D.: Major influence of tropical volcanic eruptions on the
1319 stratospheric aerosol layer during the last decade, Geophys. Res. Lett., 38,
1320 <https://doi.org/10.1029/2011GL047563>, 2011.

1321 Wang, K., Dickinson, R. E., and Liang, S.: Clear Sky Visibility Has Decreased over Land Globally from
1322 1973 to 2007, Science, 323, 1468-1470, <https://doi.org/10.1126/science.1167549>, 2009.

1323 Wang, K. C., Dickinson, R. E., Su, L., and Trenberth, K. E.: Contrasting trends of mass and optical
1324 properties of aerosols over the Northern Hemisphere from 1992 to 2011, Atmos. Chem. Phys., 12, 9387-
1325 9398, <https://doi.org/10.5194/acp-12-9387-2012>, 2012.

1326 Wei, J., Li, Z., Peng, Y., and Sun, L.: MODIS Collection 6.1 aerosol optical depth products over land and
1327 ocean: validation and comparison, Atmos. Environ., 201, 428-440,
1328 <https://doi.org/10.1016/j.atmosenv.2018.12.004>, 2019.

1329 Wei, J., Li, Z., Sun, L., Peng, Y., Liu, L., He, L., Qin, W., and Cribb, M.: MODIS Collection 6.1 3 km
1330 resolution aerosol optical depth product: Global evaluation and uncertainty analysis, Atmos. Environ.,
1331 240, 117768, <https://doi.org/10.1016/j.atmosenv.2020.117768>, 2020.

1332 Welton, E. J., Campbell, J. R., Berkoff, T. A., Spinhirne, J. D., and Starr, D. O.: The micro-pulse lidar
1333 network (MPLNET), Frontiers in Optics, <https://doi.org/10.1364/fio.2003.mk2>, 2002.

1334 Winker, D. M., Tackett, J. L., Getzewich, B. J., Liu, Z., Vaughan, M. A., and Rogers, R. R.: The global
1335 3-D distribution of tropospheric aerosols as characterized by CALIOP, Atmos. Chem. Phys., 13, 3345-
1336 3361, <https://doi.org/10.5194/acp-13-3345-2013>, 2013.

1337 Winker, D. M., Vaughan, M. A., Omar, A., Hu, Y., Powell, K. A., Liu, Z., Hunt, W. H., and Young, S. A.:
1338 Overview of the CALIPSO Mission and CALIOP Data Processing Algorithms, J. Atmos. Ocean. Tech.,
1339 26, 2310-2323, <https://doi.org/10.1175/2009jtecha1281.1>, 2009.

1340 Wu, J., Luo, J., Zhang, L., Xia, L., Zhao, D., and Tang, J.: Improvement of aerosol optical depth retrieval
1341 using visibility data in China during the past 50years, J. Geophys. Res-Atmos., 119, 13370-13387,
1342 <https://doi.org/10.1002/2014jd021550>, 2014.

1343 Xia, X., Che, H., Zhu, J., Chen, H., Cong, Z., Deng, X., Fan, X., Fu, Y., Goloub, P., and Jiang, H.: Ground-
1344 based remote sensing of aerosol climatology in China: Aerosol optical properties, direct radiative effect
1345 and its parameterization, Atmos. Environ., 124, 243-251,
1346 <https://doi.org/10.1016/j.atmosenv.2015.05.071>, 2016.

1347 Yang, X., Zhao, C., Yang, Y., and Fan, H.: Long-term multi-source data analysis about the characteristics
1348 of aerosol optical properties and types over Australia, Atmos. Chem. Phys., 21, 3803-3825,
1349 <https://doi.org/10.5194/acp-21-3803-2021>, 2021a.

1350 Yang, X., Zhao, C., Yang, Y., Yan, X., and Fan, H.: Statistical aerosol properties associated with fire
1351 events from 2002 to 2019 and a case analysis in 2019 over Australia, Atmos. Chem. Phys., 21, 3833-
1352 3853, <https://doi.org/10.5194/acp-21-3833-2021>, 2021b.

1353 Yang, X., Wang, Y., Zhao, C., Fan, H., Yang, Y., Chi, Y., Shen, L., and Yan, X.: Health risk and disease
1354 burden attributable to long-term global fine-mode particles, Chemosphere, 287,
1355 <https://doi.org/10.1016/j.chemosphere.2021.132435>, 2022.

1356 Yang, Y., Ge, B., Chen, X., Yang, W., Wang, Z., Chen, H., Xu, D., Wang, J., Tan, Q., and Wang, Z.:
1357 Impact of water vapor content on visibility: Fog-haze conversion and its implications to pollution control,
1358 *Atmos. Res.*, 256, <https://doi.org/10.1016/j.atmosres.2021.105565>, 2021c.

1359 Yoon, J., Burrows, J., Vountas, M. v., von Hoyningen-Huene, W., Chang, D., Richter, A., and Hilboll, A.:
1360 Changes in atmospheric aerosol loading retrieved from space-based measurements during the past decade,
1361 *Atmos. Chem. Phys.*, 14, 6881-6902, <https://doi.org/10.5194/acp-14-6881-2014>, 2014.

1362 Yoon, J., Pozzer, A., Chang, D. Y., Lelieveld, J., Kim, J., Kim, M., Lee, Y., Koo, J.-H., Lee, J., and Moon,
1363 K.: Trend estimates of AERONET-observed and model-simulated AOTs between 1993 and 2013, *Atmos.*
1364 *Environ.*, 125, 33-47, <https://doi.org/10.1016/j.atmosenv.2015.10.058>, 2016.

1365 Zhang, S., Wu, J., Fan, W., Yang, Q., and Zhao, D.: Review of aerosol optical depth retrieval using
1366 visibility data, *Earth-Sci. Rev.*, 200, 102986, <https://doi.org/10.1016/j.earscirev.2019.102986>, 2020.

1367 Zhang, Z., Wu, W., Wei, J., Song, Y., Yan, X., Zhu, L., and Wang, Q.: Aerosol optical depth retrieval from
1368 visibility in China during 1973-2014, *Atmos. Environ.*, 171, 38-48,
1369 <https://doi.org/10.1016/j.atmosenv.2017.09.004>, 2017.

1370 Zhao, A. D., Stevenson, D. S., and Bollasina, M. A.: The role of anthropogenic aerosols in future
1371 precipitation extremes over the Asian Monsoon Region, *Clim. Dynam.*, 52, 6257-6278,
1372 <https://doi.org/10.1007/s00382-018-4514-7>, 2019.

1373